ANALYSIS OF A MINIATURE RADIO FREQUENCY ION THRUSTER WITH AN INDUCTIVELY COUPLED PLASMA SOURCE

by

Peter Paul Bumbarger

A thesis

submitted in partial fulfillment

of the requirements for the degree of

Master of Science in Electrical Engineering

Boise State University

December 2013

BOISE STATE UNIVERSITY GRADUATE COLLEGE

DEFENSE COMMITTEE AND FINAL READING APPROVALS

of the thesis submitted by

Peter Paul Bumbarger

Thesis Title: Analysis of a Miniature Radio Frequency Ion Thruster with an Inductively Coupled Plasma Source

Date of Final Oral Examination: 13 September 2013

The following individuals read and discussed the thesis submitted by student Peter Paul Bumbarger, and they evaluated his presentation and response to questions during the final oral examination. They found that the student passed the final oral examination.

Jim Browning, Ph.D.	Chair, Supervisory Committee
Wan Kuang, Ph.D.	Member, Supervisory Committee
Don Plumlee, Ph.D., P.E.	Member, Supervisory Committee

The final reading approval of the thesis was granted by Jim Browning, Ph.D., Chair, Supervisory Committee. The thesis was approved for the Graduate College by John R. Pelton, Ph.D., Dean of the Graduate College.

For my parents, Connie and Donald

ACKNOWLEDGMENTS

There are many people that helped in many different ways to make this thesis possible.

First, I thank Dr. Jim Browning and Dr. Don Plumlee for the opportunity to work with the Electric Propulsion Research Group at Boise State University. I would like to thank the Electrical and Computer Engineering Department Head, Dr. Sin Ming Loo, and the Dean of the College of Engineering, Dr. Amy Moll, for providing a wonderful environment to perform research.

I would like to thank the members of my defense committee: Dr. Jim Browning, Dr. Wan Kuang, and Dr. Don Plumlee. Thank you for taking time to review and provide feedback for this thesis.

I am grateful for my friend, roommate, and colleague, Mahesh Ailavajhala for convincing me to move to Idaho for graduate school at Boise State and for introducing me to Dr. Browning. I would not be here if it was not for you.

Many thanks to the members of the Electric Propulsion Research Group; past and present.

I wish to thank Jake Morison and Alfredo Bravo Iñiguez for developing models of the miniature ion thruster in order to optimize the design for the ion optics.

Thank you Jesse Taff, Kelci Parish, Mallory Yates, Deb French, and Logan Knowles for building various parts of the miniature ion thruster over the past few years.

I would also like to thank Jack Woldvedt for designing, fabricating, and testing the micronewton thrust measurement stand.

Thank you Carl Lee for developing the LabView Data Acquisition and control system.

Thank you Derek Reis and Mike Rippee for upgrading the LabView vi.

Thank you Janos Cserna, Marcus Pearlman, and Kyle Straub for designing, building, and debugging the opto-isolator boards.

Thank you Sonya Christensen for all your hard work designing an optimized ICP source.

I also wish to thank Sonya Christensen, Sulmer Fernández-Gutierrez, Marcus Pearlman, and Tyler Rowe for always being available to bounce off ideas from theory to implementation in the lab.

Finally, I wish to thank my parents Connie and Donald Bumbarger for always supporting and encouraging me to pursue challenging problems. Who would have thought that my first model rocket would lead to this?

Ex astris, scientia.

This work was made possible by NASA EPSCoR Award NNX09AV04A, material donation by DuPont, and the Boise State University Department of Electrical and Computer Engineering.

AUTOBIOGRAPHICAL SKETCH

Peter Bumbarger graduated from North Star High School in Boswell, Pennsylvania on June 6, 2005. He then started studying electrical engineering at the Pennsylvania State University in June of 2005.

While at Penn State, he worked in the Student Space Programs Lab, a multidisciplinary lab that allows undergraduate and graduate students to experience the complete design cycle for space systems. He served as communications lead on NittanySat, a small satellite and Penn State's entry in the University NanoSat V Program. He graduated from Penn State on May 15, 2009 with a BSEE and a certificate in Space Systems Engineering.

Peter was employed by Northrop Grumman as a field engineer from July of 2009 to September of 2010. He worked on the Flats Sequencing System (FSS), a revolutionary mail automation system for the United States Postal Service that sorts various flat mail pieces in delivery point order. He was involved with system validation, installation, operation, and retrofitting.

In April of 2011, Peter moved to Boise, Idaho to begin work as a graduate research assistant with the Electric Propulsion Group at Boise State Univeristy. He is a graduate student member of the Institute of Electrical and Electronics Engineers (IEEE) and belongs to the Nuclear and Plasma Science, Aerospace and Electronic Systems, and Communications Societies. He is a member of Eta Kappa Nu (HKN), the electrical and computer engineering honor society. He is also a graduate student member of the American Institute of Aeronautics and Astronautics (AIAA).

ABSTRACT

The performance of a 2 cm miniature ion thruster was analyzed. A thruster of this size was predicted to produce a thrust of 200 μN. The plasma density was measured against rf input power and propellant flow rate for three configurations: the ICP source by itself; the ICP source with discharge chamber; and finally, the ICP source, the discharge chamber, and the permanent magnet cusp system. Once the optimum case was determined, electrostatic grids were added and thrust measurements were taken with a set of segmented ion collector plates.

The miniature rf ion thruster obtained a thrust of 22.35 μN and a specific impulse of 15.31 s at its optimum operating condition of 5 W of rf power and and propellant flow rate of 5 sccm. With a beam divergence angle of 26.25° and the assumption of a singly charged ion species, the total thrust correction factor was 0.90. The mass utilization efficiency of the thruster was calculated to be 0.24 %. The electrical efficiency of thruster was calculated to be 16.94 % with an electron-ion energy pair cost of 5.9 keV/ion. The total efficiency of the thruster was 0.033 %, a factor of 1000 too low for practical use.

TABLE OF CONTENTS

LIST OF TABLES

LIST OF FIGURES

LIST OF ABBREVIATIONS

amu – atomic mass unit

CAD – Computer Aided Design

CCP – Capacitively Coupled Plasma

coax – coaxial cable

DAQ – Data AcQuisition

EP – Electric Propulsion

EPROP – Electric Propulsion Group at Boise State University

ESA – European Space Agency

GPIB – General Purpose Interface Bus

GOCE – Gravity field and steady-state Ocean Circulation Explorer

HV – High-Voltage

I-V – current-voltage

ICP – Inductively Coupled Plasma

JAXA – Japanese Aerospace eXploration Agency

JPL – Jet Propulsion Laboratory

LTCC – Low Temperature Co-Fired Ceramic

MFC – Mass Flow Controller

NASA – National Aeronautics and Space Administration

NSSK – north-south station keeping

NSTAR – NASA Solar Technology Application Readiness

PIT – Pulsed Inductive Thruster

rf – Radio Frequency

sccm – Standard Cubic Centimeter per Minute

SMA – SubMiniature version A

TCP – Transformer Coupled Plasma

vi – Virtual Instrument

LIST OF SYMBOLS

a probe radius (m)

B magnetic flux density (T)

d probe length (m)

e elementary charge (C)

g acceleration due to gravity (m/s^2)

h altitude above sea level (m)

I^+ ion current due to singly charged ions (A)

I^{++} ion current due to doubly charged ions (A)

I_a screen grid current (A)

I_b ion beam current (A)

I_s screen grid current (A)

I_{sp} specific impulse (s)

I_{total} total current (A)

I_θ ion beam current at angle θ (A)

J current density (A/m^2)

J_{total} total ion beam current density (A/m^2)

J_θ ion beam current density at angle (A/m^2)

k Boltzmann constant (1.38×10^{-23} J/K)

$^{L}/_{D}$ length-to-diameter ratio

m_0 initial mass (kg)

m_1 final mass (kg)

m_d delivered mass (kg)

$\dot{m}_{Ar}$ mass flow rate of argon (sccm)

$\dot{m}_i$ ion mass flow rate (kg/s)

$\dot{m}_N$ mass flow rate of nitrogen (sccm)

$\dot{m}_p$ propellant mass flow rate (kg/s)

m_e electron mass (kg)

m_i ion mass (kg)

m_p propellant mass (kg)

n_0 bulk plasma density (m^{-3})

n_s sheath plasma density (m^{-3})

p_0 atmospheric pressure at sea level (101.325 kPa)

p_{Ar} argon pressure (Torr)

$\bar{p}$ mean atmospheric pressure (Pa)

p_g gauge pressure (Torr)

P_b beam power (W)

P_{in} input power (W)

P_{IO} ion optics power (W)

P_{jet} jet power (W)

P_{rf} rf power (W)

q charge (C)

r_c Larmor radius (m)

s plasma sheath thickness (m)

T Thrust (N)

T temperature (K)

V_B probe bias voltage (V)

V_b net ion acceleration voltage (V)

v_{ex} exhaust velocity (m/s)

v_i ion velocity (m/s)

$v_\perp$ particle perpendicular velocity (m/s)

α maximum angle between the collector and the thrust axis (°)

α_{div} thrust correction factor due to ion beam divergence

α_i thrust correction factor due to doubly ionized ions

γ total thrust correction factor

Δv delta-v, change in velocity (m/s)

ε_B electron-ion pair energy cost (W/A = eV/ion)

η_e electrical efficiency

η_m mass utilization efficiency

η_T total efficiency

θ angle between the collector and the thrust axis (°)

Φ_p plasma potential (V)

χ figure of merit

ω_c cyclotron frequency (rad/s)

CHAPTER 1

INTRODUCTION

The cost to lift payloads into low earth orbit is approximately $\$10,000\,/\text{lb}$ [1]. Because of this high cost, significant efforts have been made in recent years to scale down satellite payloads to what are known as small satellites. Small satellites are satellites with a mass less than 500 kg. Classifications of satellites based on mass and manufacturing cost are summarized in Table 1.1[1]. Small satellites have been used for specialized communications services and research, Earth observation and remote sensing, small-scale space science, in-space technology demonstration and verification, and education and training [3].

Table 1.1: Classification of Satellites [3]

Class		Mass (kg)	Cost (US $ million)
large		> 1000	> 181.72
medium		$500 - 1000$	$64.90 - 181.72$
small	mini	$100 - 500$	$12.98 - 38.94$
	micro	$10 - 100$	$3.89 - 7.79$
	nano	$1 - 10$	$0.39 - 1.95$
	pico	< 1	< 0.39

As small satellites become more popular, a means for a micro-propulsion system is needed. These satellites inherently have limited volume and mass budgets that make conventional chemical propulsion impractical due to the amount of propellant needed

[1]Table values are adjusted for 2013 USD [2].

to accomplish mission objectives. Electric propulsion (EP) is a viable alternative for orbital systems. EP is a proven method of in-space propulsion for spacecraft [4–6]. EP offers high specific impulse with the engineering tradeoff of low thrust as compared to conventional chemical rockets that have low specific impulse and high thrust. EP is a solution because of its efficient use of propellant and because of its long lifetime. Current flight heritage ion engines are quite large, relative to small satellites. The goal of this research is to scale down an electrostatic ion engine that can be used on a small satellite. The terms motor, engine, thruster, and rocket may be used interchangeably throughout this thesis; all terms refer to a device that creates a reactionary force as a means for a propulsion.

1.1 A Brief History of Ion Thrusters

The first known proposal for the use of charged particles to increase exhaust velocities for rockets was in 1906 in the notebook of American rocket pioneer, Robert Hutchings Goddard [7]. Goddard experimented with ion sources and with what he called "electrified jets," which were chemical rocket jets injected with ions. This work eventually culminated in US patent 1363037 filed in 1917 and issued in 1920. Figure 1.1 shows what is considered to be the first documented electrostatic ion thruster.

Konstantin Eduardovitch Tsiolkovsky also played an early role in electric propulsion. Tsiolkovsky was a self-taught Russian rocket scientist and is most famous for formulating the Tsiolkovsky Rocket Equation (see Section 2.2.1) in 1903. Tsiolkovsky wrote briefly on electric propulsion in his 1911 work, *The Investigation of the Universal Space by Means of Reactive Devices* [9]:

> It is possible that in time we may use electricity to produce a huge velocity

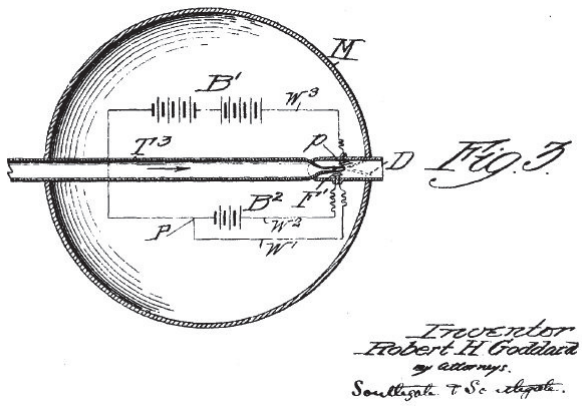

Figure 1.1: First known documented electrostatic ion thruster by Robert H. Goddard in US Patent 1363037 (1920) [8].

> for the particles ejected from the rocket device. It is known at the present that the cathode rays in Crookes' tube, just like the rays of radium, are accomplished by a flux of electrons whose individual mass is 4,000 times less than the mass of the helium atom, while the velocities obtained are 30,000-100,000 km/sec, i.e., 6,000 to 20,000 times greater than the velocity of the ordinary products of combustion flying from our reactive tube. [9]

Both Goddard and Tsiolkovsky decided to devote their studies to chemical propulsion because it seemed to be a more feasible undertaking at the time. As of 1929, the EP work of Goddard and Tsiolkovsky was mostly forgotten [10].

Hermann Julius Oberth wrote a chapter on electric propulsion in his 1929 book *Wege zur Raumschiffahrt* (Ways to Spaceflight) entitled [11], *Das elekrische Raumschiff* (The Electric Space-Ship). He explores both spacecraft power and EP. EP is suggested for use as attitude control and deep space propulsion. Unlike Goddard and Tsiolkovsky, Oberth's work was instantly popular with scientists and science fiction writers [10]. Oberth concludes his book with:

> Whether all this will work, I do not know. But nothing is impossible on earth; one must only discover the means with which it can be carried out. [11]

In 1947, after being relocated to the United States by Operation Paperclip, German rocket scientist Wernher von Braun asked his colleague Ernst Stuhlinger to investigate electric propulsion further, stating,

> Professor Oberth has been right with so many of his early proposals; I wouldn't be a bit surprised if one day we flew to Mars electrically! [12]

Stuhlinger would spend the next decade researching the electrostatic ion thruster. Harold R. Kaufman then lead the development of the first ion engine to be used in space at Lewis Research Center (now Glenn Research Center) from 1957 to 1964. Figure 1.2 shows a schematic of an electron-bombardment thruster that Kaufman developed [13].

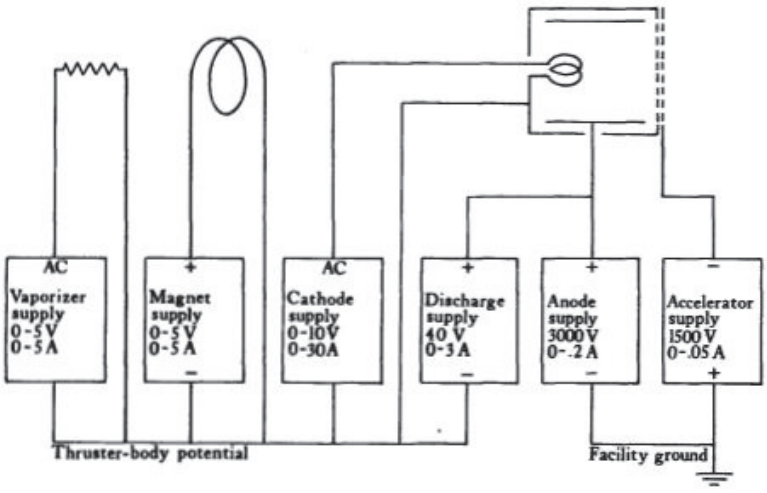

Figure 1.2: Schematic of a electron-bombardment thruster developed by Harold R. Kaufman [13].

The first ion engine that operated in space was flown on the National Aeronautics and Space Administration (NASA) Space Electric Rocket Test I (SERT-I) in 1964. Two different ion engines were flown on SERT-I: a mercury-bombardment ion engine and a cesium-contact ion engine. The mercury-bombardment ion engine was operational for 31 min 16 s during the 46 min 58 s ballistic flight. The cesium-contact ion engine did not operate because of a high-voltage (HV) electrical short circuit. The flight proved that the neutralizer system worked and that thrust could be produced with no major differences from what was observed in vacuum chamber tests [4].

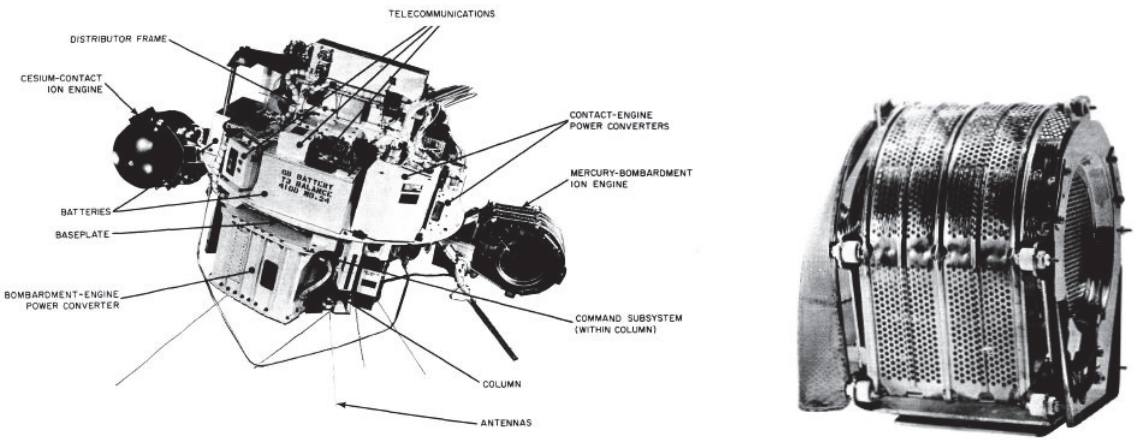

(a) (b)

Figure 1.3: (a) SERT-I spacecraft with subsystems labeled and (b) a close-up of mercury-bombardment ion engine, the first use of electric propulsion in space in 1964 [14].

The first NASA mission to use an ion engine as a primary propulsion system was the Jet Propulsion Laboratory's (JPL) Deep Space 1 Probe in 1999 [15]. Figure 1.4 is a photograph of the NASA Solar Technology Application Readiness (NSTAR) engine firing in a vacuum chamber at JPL. Both the European Space Agency (ESA) [5, 16] and Japanese Aerospace Exploration Agency (JAXA) [17] have also used electric propulsion on spacecraft. A German rf ion thruster, called the RIT-10, was used

on the ESA ARTEMIS geostationary communication satellite [5]. When ARTEMIS was launched, the upper stage of the Ariane 510 failed and left ARTEMIS in a much lower than intended elliptical orbit. The RIT-10, which was originally intended for north-south station keeping (NSSK), raised ARTEMIS to geostationary orbit and saved the mission [18]. The ESA also used the T5 ion engine on the Gravity Field and Steady-State Ocean Circulation Explorer (GOCE) spacecraft [16]. JAXA used a microwave source ion engine, called the μ10, on the Hayabusa near-Earth asteroid mission [17].

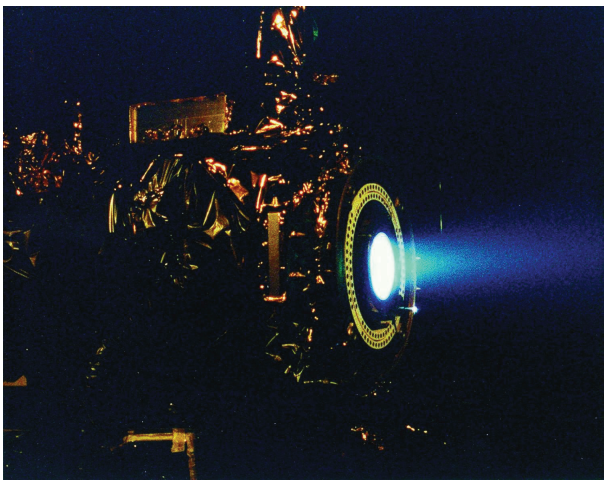

Figure 1.4: Photograph of Deep Space One's NSTAR ion engine firing in a vacuum chamber [19].

Currently, JPL's Dawn Mission is using ion propulsion to explore the asteroid Vesta and the dwarf planet Ceres in the asteroid belt. Dawn is using the NSTAR ion engine, which was previously used on the Deep Space 1 Probe [6]. As of September 2012, Dawn has fired its ion engine to leave Vesta and is en route to Ceres with an estimated time of arrival of early 2015 [20]. Figure 1.5 shows an artist's depiction of the Dawn spacecraft departing Vesta [21].

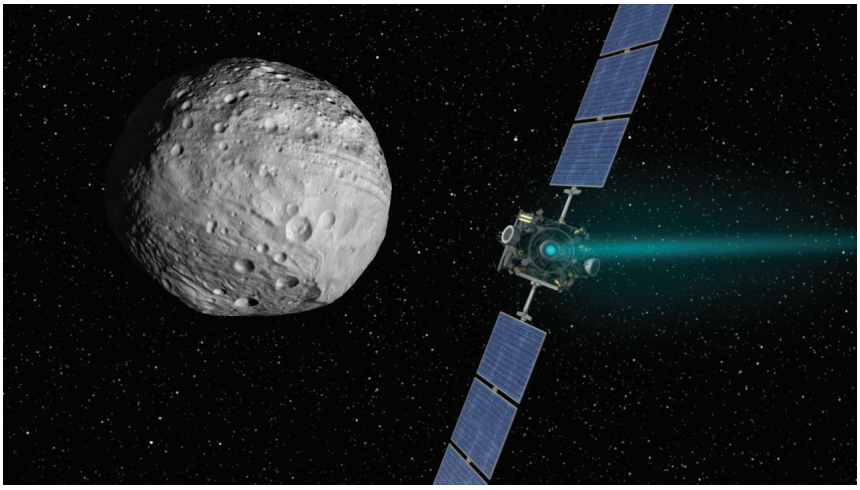

Figure 1.5: An artist's depiction of NASA's Dawn spacecraft's departure of asteroid Vesta [21].

1.2 Previous Work on Miniature Ion Thrusters

1.2.1 California Institute of Technology and Jet Propulsion Laboratory Electron Bombardment Micro-Ion Thruster

Research on the scaling down of ion thrusters has become an area of interest in recent years due to the ever increasing popularity of small satellites. Caltech and JPL have developed an electron bombardment micro-ion thruster [22] with a 3 cm diameter. Different geometries for the discharge chamber and magnetic cusp were investigated in order to find the most efficient configuration. A maximum total efficiency of 43.5 % was obtained with a divergent axial geometry with a length-to-diameter ratio of 0.75 [22]. For this configuration, a thrust of 0.88 mN was obtained [22].

1.2.2 The Pennsylvania State University MRIT

A miniature radio-frequency (rf) ion thruster (MRIT) was developed at the Pennsylvania State University [23]. MRIT has a diameter of 1 cm [24]. The MRIT was able

to obtain 59 μN of maximum thrust and a specific impulse of 5480 s [24]. MRIT had a mass utilization efficiency of 79.1 % and an electrical efficiency of 15.2 % [24].

1.2.3 Giessen University μNRIT 4 and μNRIT 2.5

Giessen University in Germany has been working on scaling down the RIT ion engine [25]. The μNRIT-4 thruster has a 4 cm diameter. Two versions of this thruster were constructed: the μNRIT 4/151 with 151 holes for ion extraction and the μNRIT-4/7 with seven holes for ion extraction. The μNRIT 4/151 has a thrust range from 150 μN to 3.5 mN. At maximum thrust, the mass utilization efficiency was 80 % and the electrical efficiency was 60 % with a power-to-thrust ratio of 40 W/mN [25]. The μNRIT 4/7 has a thrust range from $< 10\,\mu$N to 200 μN. The efficiencies were similar to that of the μNRIT 4/151 [25].

Giessen Univeristy has also developed a 2.5 cm diameter ion thruster known as the μNRIT 2.5. The μNRIT 2.5 with 37 extraction holes had a thrust range of 200 μN to 500 μN. The mass utilization efficiency ranged from $29.9 - 49.1$ % and the electrical efficiency ranged from $21.6 - 42.6$ % [26].

1.2.4 QinetiQ and University of Southampton Differential Radio Frequency Ion Thruster

Collaboration between QinetiQ and the University of Southampton in the United Kingdom produced a differential radio frequency ion thruster [27]. The thruster has an internal diameter of 3.3 cm. The thruster is referred as a differential thruster because it is able to thrust in both the positive and negative directions of its thrust axis. A thrust range from 200 μN to 480 μN was produced with 22 W to 29 W of rf

power with xenon propellant flow rates of $0.03\,\mathrm{mgs}^{-1}$ to $0.05\,\mathrm{mgs}^{-1}$ (0.3076 sccm to 0.5126 sccm) [27]. These examples of previous work are summarized in Table 1.2.

Table 1.2: Summary of Previous Work

	Caltech and JPL Micro-Ion Thruster	Penn State University MRIT	Giessen University μNRIT 4	University of Southampton and QinetiQ Differential Thruster
diameter	3 cm	1 cm	4 cm	3.3 cm
thrust	0.88 mN	59 μN	3.5 mN	480 μN
η_e	N/A	15.2 %	60 %	21.6 – 42.6 %
η_m	N/A	79.1 %	80 %	29.9 – 49.1 %

1.3 Thesis Outline

In order to become practical for use in space, the efficiencies of these miniature thrusters must be increased significantly. The objective of this thesis is to analyze and optimize the performance of a new miniature ion thruster that can be integrated for use on a small satellite.

Chapter 2 gives a background on plasma and rocket theory. Several methods of plasma generation are described in this chapter. The Tsiolkovsky Rocket Equation is discussed in this chapter to illustrate the advantages of electric propulsion over chemical propulsion. The thrust equation for an ideal electrostatic ion thruster is derived in order to calculate the theoretical maximum thrust that can be produced by a miniature ion thruster. Thrust corrections are added to compensate for ion beam divergence and the presence of multiply charged ion species. Details of the design and fabrication process of the miniature ion thruster in this research are also discussed in this chapter.

The design of the miniature rf ICP ion thruster is discussed in Chapter 3. This chapter summarizes the fabrication and performance of multiple ICP antennas of varying geometries from previous work [28, 29]. Dimensions of the thruster chamber and placement of magnets are explored from previous work on a 3-cm ion bombardment engine. The design and fabrication of the ion optics of the electrostatic grids are discussed.

In Chapter 4, an overview of the experiment set up used to conduct all of the experiments in this research is provided. This discussion includes the rf antenna, propellant delivery, pressure control, throttle control, Langmuir probe, and the thrust measurement systems.

Chapter 5 contains experimental results. Plasma density is compared versus the flow of propellant, rf power, and background pressure. Thrust is measured electrically through the use of segmented ion collector plates. The mass utilization, electrical, and total thruster efficiencies as well as the electron-ion pair energy cost are calculated for the miniature ion thruster.

Finally, Chapter 6 contains a summary of the work done, conclusions, and suggestions for future work.

CHAPTER 2

BACKGROUND

This chapter will discuss the properties of plasma, the methods of plasma generation, the meaning of the Tsiolkovsky rocket equation, and the differences between chemical and electric rockets. Equations for thrust and specific impulse are derived for an electrostatic ion thruster.

2.1 Plasma

Plasma is known as the fourth state of matter and constitutes 99.9% of the visible universe [30]. Plasmas occur naturally in space and in the atmosphere, such as nebulae, stars, lightning, and aurora. Plasmas can also be man-made, such as those used in fluorescent lighting, neon signs, high voltage electrical arcs, and semiconductor processing. Put simply, plasma is an excited, or ionized gas. It is comprised of positively and negatively charged particles of approximately equal densities. Therefore, on average, a plasma is macroscopically neutral. When an atom of a neutral gas is ionized, an electron is separated from the atom and the atom becomes a positively charged ion. Different types of low pressure plasma discharges are described below.

2.1.1 DC Glow Discharge

One of simplest types of plasma discharges is the dc glow discharge. As shown in Figure 2.1, a dc glow discharge plasma is generated when a current is carried by a low pressure gas between an anode and a cathode. A potential of several hundred volts between these electrodes is required to sustain the discharge in a pressure range of 10 mTorr to 10 Torr [31]. Figure 2.1 shows a schematic [31] of a dc glow discharge and plots of light intensity, potential distribution, field strength, net space charge, negative charges, and positive charges versus position. The dc glow discharge consists of nine regions: the anode dark space, anode glow, positive column, Faraday dark space, negative glow, Crookes dark space, cathode glow, and Aston dark space. The dc glow discharge is sustained by electron impact ionization of neutral atoms and secondary electron emission from ions impacting the cathode.

2.1.2 Capacitive Discharge

When an rf current is carried by a low pressure or atmospheric gas between two electrodes, a capacitively coupled plasma (CCP) is formed [32]. A schematic of a CCP discharge is shown in Figure 2.2. A plasma sheath forms at at each electrode. Unlike a dc glow discharge, both displacement current and conduction current sustain the discharge [32]. The plasma is heated by ohmic heating in the bulk plasma and stochastic heating in the sheath. The electrodes are often exposed to the plasma and are susceptible to sputtering by ion bombardment. In semiconductor processing, CCP are driven by 50 Ω rf sources typically at 13.56 MHz. However, other frequencies are used.

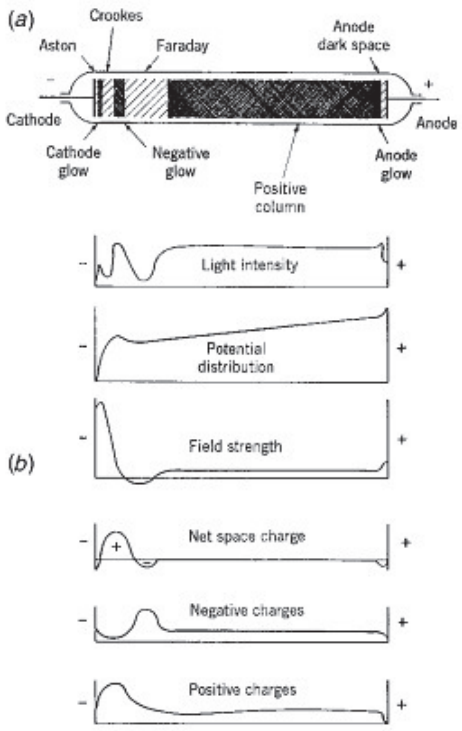

Figure 2.1: Schematic of a dc glow discharge and profiles of discharge properties versus position [31].

2.1.3 Inductive Discharge

In an inductively coupled plasma (ICP), the rf energy is coupled to free electrons via magnetic induction (Faraday's Law). An inductively coupled plasma source uses rf waves from 100 kHz to 1 GHz to generate and sustain a plasma. This is most commonly accomplished with a planar or cylindrical coil antenna where the antenna is insulated with a dielectric material (see Figure 2.3).

Unlike other types of discharges, electrodes are not exposed to the plasma. The ICP discharge can be modeled as a *transformer*. In Figure 2.4, R_p and L_p represent the impedance of the plasma while R_s and L_s represent the impedance of the ICP source. L_{11} and L_{22} represent the inductance of the *transformer* [33]. These types of

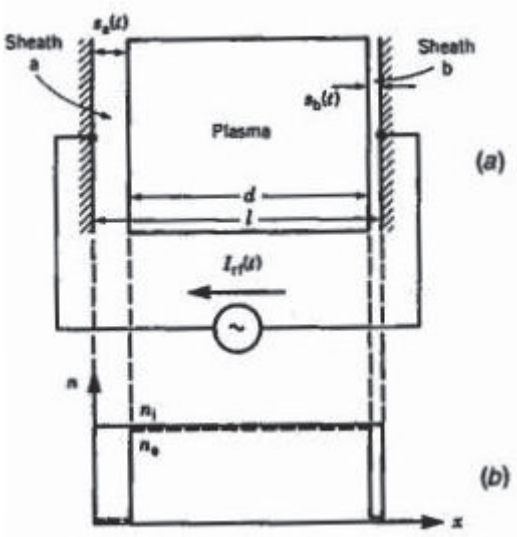

Figure 2.2: Schematic and profile density of a CCP discharge [32]. An rf current source is applied to two electrodes with a neutral gas between the electrodes. In steady-state, a plasma sheath is formed at each electrode.

sources are also called transformer coupled plasma (TCP) sources.

In order to efficiently transfer maximum power to the plasma, a matching network must be placed into the circuit between the ICP source and the rf source. In Figure 2.5, a series capacitor C_1 and a shunt capacitor C_2 are added the equivalent circuit model in order to tune the circuit to a particular frequency. R_T is the line impedance and V_{rf} is the rf source. The matching needed to initiate the plasma (gas without plasma) is different than that needed to sustain the plasma.

An example of the inductively coupled plasma discharge used in this research is shown in Figure 2.6. A planar spiral antenna was placed on a Teflon test stand that allows injection of argon gas. A plasma was generated with 20 W of rf power at a background argon pressure of 100 mTorr.

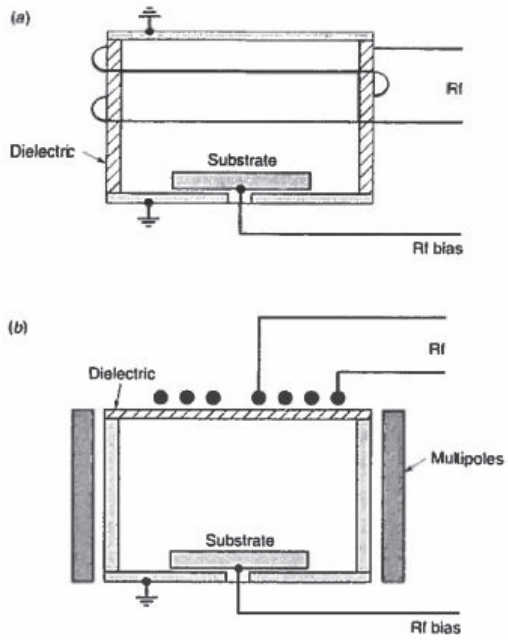

Figure 2.3: (a) Cylindrical and (b) planar spiral configurations of an ICP discharge [33]. An rf current is supplied to the coil and energy is coupled to free electrons via magnetic induction.

2.2 Rockets

2.2.1 The Tsiolkovsky Rocket Equation

Delta-v (Δv) is the change in velocity a rocket must make in order accomplish a specific task. These tasks may include carrying a payload to low earth orbit from the surface, changing orbits, attitude control, and deep space cruising. Konstantin Tsiolkovsky realized that Δv of a rocket was a function of the propellant exhaust velocity, initial mass, and final mass. Tsiolkovsky formulated this relation in his 1903 work, *A Rocket into Cosmic Space* [9].

$$\Delta v = v_{ex} \ln \frac{m_0}{m_1} = I_{sp} g \ln \frac{m_d + m_p}{m_d}, \tag{2.1}$$

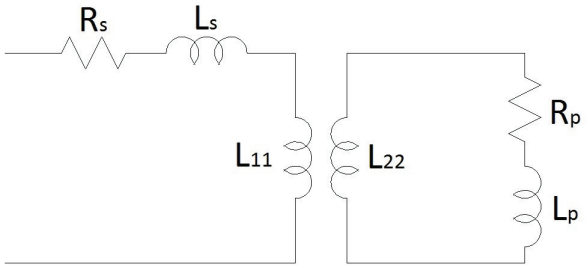

Figure 2.4: Equivalent circuit model of an inductively coupled discharge

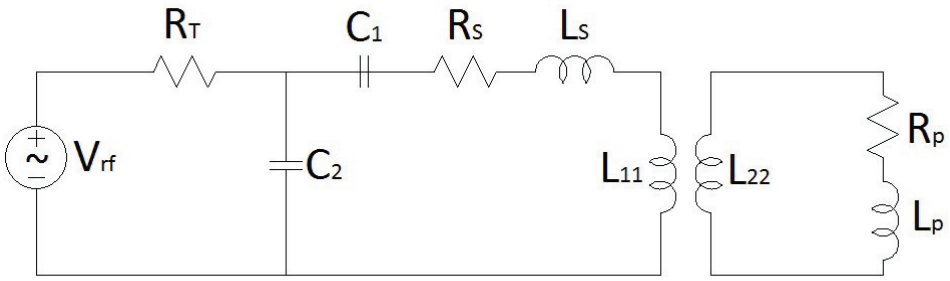

Figure 2.5: Equivalent circuit model of an inductively coupled discharge matched to an rf power source.

where Δv is delta-v, the change in velocity (m/s), v_{ex} is the exhaust velocity (m/s), m_0 is the initial mass of the rocket (kg), m_1 is the final mass of the rocket (kg), I_{sp} specific impulse (s), g is acceleration due to gravity (m/s^2), m_d is delivered mass (kg), and m_p is propellant mass (kg). Take note that $v_{ex} = I_{sp} \cdot g$. Equation (2.1) can be rewritten as:

$$m_p = m_d \left(e^{\Delta v / I_{sp} \cdot g} - 1 \right). \tag{2.2}$$

When the exhaust velocity is much greater than the required delta-v for a given mission objective, the amount of propellant needed is greatly reduced. Since $I_{sp} = \frac{v_{ex}}{g}$,

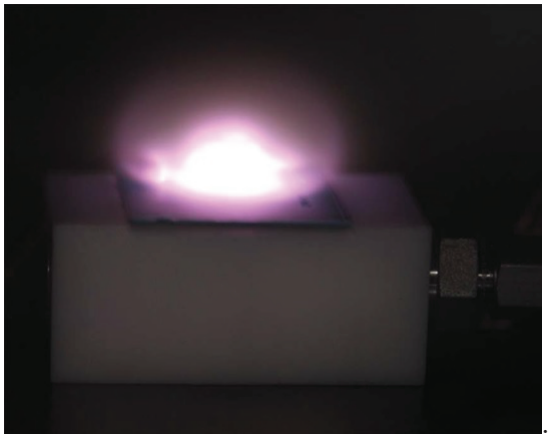

Figure 2.6: An inductively coupled plasma discharge with argon gas using a flat spiral antenna (1.5 cm diameter) on a ceramic substrate with an Ar pressure of 100 mTorr and an rf power of 20 W [34].

the greater the exhaust velocity of a rocket, the greater the specific impulse. High specific impulse translates to lower required propellant mass. Specific impulse is also used as a metric to gauge the efficiency of ion engines.

2.2.2 Chemical Rockets Versus Electrical Rockets

Chemical rockets use the expansion of hot gases accelerated through a converging-diverging nozzle to create thrust. Fuel and oxidizer are added to the combustion chamber by either a pressure feed or pump system. The hot gases formed from combustion are then accelerated through the rocket nozzle because of the pressure against the walls of the combustion chamber. A schematic of a liquid bipropellant rocket engine is shown in Figure 2.7. Fuel and oxidizer are added to the combustion chamber through a turbopump and valve system.

Just as traditional rockets use chemical reactions to accelerate propellant to high exhaust velocities, electric propulsion systems accelerate charged particles through the use of electric fields to create thrust. Because charged particles are subjected to

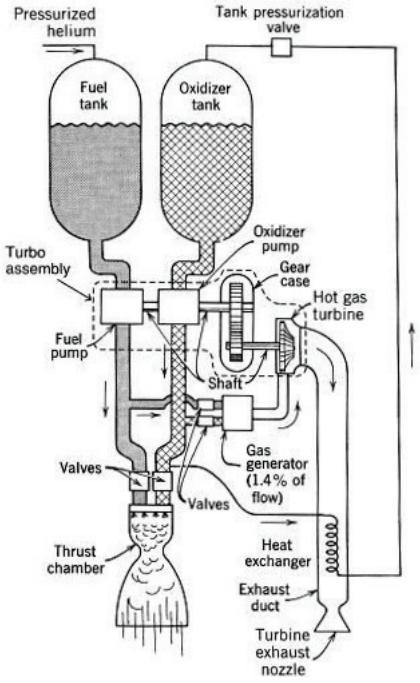

Figure 2.7: Schematic of a liquid bipropellant propellant chemical rocket [35].

high electric fields, ion engines are capable of much higher exhaust velocities.

In the case of the electrostatic ion thruster, a plasma is generated and positively charged ions are extracted from the plasma through the use of an electrostatic grid system. The simplest grid system consists of a screen grid and an accelerator grid. The screen grid is the grid closest to the plasma and is biased slightly less positive than the plasma potential (approximately 1000 V). The accelerator grid is biased a few hundred volts negative (approximately -200 V with respect to the thruster chamber). The accelerator grid is biased negative in order to prevent electrons from the neutralizer from being attracted to the accelerator grid. This voltage difference causes the ions to accelerate through a potential of approximately 1200 V and creates an exhaust velocity of several thousand meters per second. A beam of electrons is emitted to neutralize the beam of ions, producing a net acceleration of 1000 V relative

to the 0 V space potential. The ion beam is neutralized to prevent charging of the spacecraft. A schematic of a miniature rf ion thruster is shown in Figure 2.8. Take note that the ion beam neutralizer is not shown in this schematic.

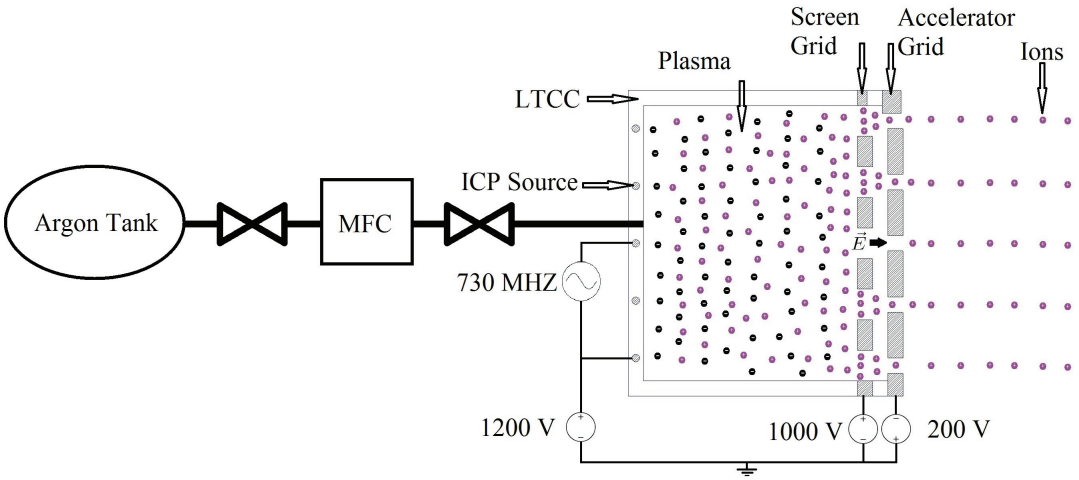

Figure 2.8: Schematic of the miniature rf ion thruster used in this research. Argon gas is delivered to the discharge chamber through a mass flow controller (MFC). A 700 MHz source is applied the ICP source. Plasma is generated and sustained by the ICP source rf energy via magnetic induction. The screen grid is biased at 1000 V in order to confine the plasma to the discharge chamber. The accelerator grid is biased at −200 V. This potential difference between the two grids accelerates argon ions to high velocities in order to produce thrust. The neutralizer is not shown.

2.2.3 Thrust for Electrostatic Ion Thrusters

Ideal Thrust

Thrust is the reactionary force that propels a rocket forward. Thrust is defined as [36]:

$$T = \frac{dm_p}{dt} v_{ex} = \dot{m}_p v_{ex}, \tag{2.3}$$

where T is thrust (N) and $\dot{m}_p$ is the mass flow rate of propellant (kg/s).

In the case of an ion thruster, the mass flow rate of propellant and exhaust velocity can be approximated to the mass flow rate of ions and the velocity of ions, respectively. Thrust can now be written as

$$T = \dot{m}_p v_{ex} \approx \dot{m}_i v_i, \tag{2.4}$$

where $\dot{m}_i$ is the ion mass flow rate (kg/s) and v_i is the ion velocity (m/s). The ion mass flow rate is written as:

$$\dot{m}_i = \frac{I_b m_i}{q}, \tag{2.5}$$

where I_b is the ion beam current, m_i is ion mass (kg), and q is the charge of the ion (C). The ion velocity is described as:

$$v_i = \sqrt{\frac{2qV_b}{m_i}}, \tag{2.6}$$

where V_b is the net ion acceleration voltage (V).

Substituting Equations (2.5) and (2.6) into (2.4) and replacing the charge q with the elementary charge e, Equation (2.4) becomes

$$T = \sqrt{\frac{2m_i}{e}} I_b \sqrt{V_b}. \tag{2.7}$$

Argon is used in the experiments presented here, so using the atomic mass of argon, 39.948 amu, and the mass of the proton, $1.67262158 \times 10^{-27}$ kg, the mass of an argon ion is 6.68179×10^{-26} kg. For argon, $\sqrt{\frac{2m_i}{e}} = 9.13285 \times 10^{-4}$, which makes Equation (2.7) reduce to

$$T = 913.285 I_b \sqrt{V_b} \qquad [\mu\text{N}] \qquad (\text{for argon})\,, \tag{2.8}$$

where V_b is the net ion acceleration voltage (V). Similarly, if xenon is used as the propellant, an atomic mass of 131.293 amu is used and equation (2.7) becomes

$$T = 1655.8 I_b \sqrt{V_b} \qquad [\mu\text{N}] \qquad (\text{for xenon})\,. \tag{2.9}$$

The total thrust is limited due to the space charge condition described by the Child-Langmuir Law [37],

$$J = \frac{4\varepsilon}{9} \left(\frac{2e}{m_i}\right)^{1/2} \frac{V_b^{3/2}}{s^2}, \tag{2.10}$$

where J is the current density (A/m^2) and s is the plasma sheath thickness (in this case electrostatic grid separation distance) (m). Using $s = 2\,\text{mm}$ and $V_b = 1000\,\text{V}$, the maximum current density that can be produced by the thruster is $68.2\,\text{A/m}^2$, which translates to a maximum current of 21.4 mA. Inserting this result into equation (2.8) yields a maximum theoretical thrust of $618.6\,\mu$N. The project goal of $200\,\mu$N is feasible.

Thrust Correction Factors

It is important to note that equations 2.7, 2.8, and 2.9 are ideal equations for thrust, i.e. the equations assume that particles travel only in the axial direction with no radial velocity components and that there is only singly charged ion species.

Depending on the ion optics, the ions will have a radial velocity in addition to an axial velocity. This creates a beam divergence. The thrust correction factor due to

divergence of the ion beam is [38]:

$$\alpha_{div} = \frac{1}{I_{total}} \sum_{\theta=0}^{\theta=\alpha} I_\theta \cos\theta, \tag{2.11}$$

where α_{div} is the thrust correction factor due to the ion beam divergence, α is maximum angle between the collector and the thrust axis, θ is the angle between the collector and the trust axis, I_{total} is the sum of all currents on the collector, and I_θ the is the ion beam current at angle θ. If current density is measured in the radial direction, Equation 2.11 becomes

$$\alpha_{div} = \frac{1}{J_{total}} \sum_{\theta=0}^{\theta=\alpha} J_\theta \cos\theta \tag{2.12}$$

where J_{total} is the sum of all current densities (A/m^2) on the collector and J_θ is the current density (A/m^2) at angle θ.

Another correction needs to be applied for the presence of multiply charged ion species. Singly charged ions can undergo another collision and lose another electron to become doubly charged. The correction factor for the presence of doubly charged ions is given by

$$\alpha_i = \frac{I^+ + \frac{1}{\sqrt{2}} I^{++}}{I^+ + I^{++}}, \tag{2.13}$$

where α_i is the thrust correction factor due to doubly ionized ions, I^+ is the ion current from singly charged ions (A), and I^{++} is the ion current from doubly charged ions (A). Note that if there is no ion current from doubly charged ions, $\alpha_i = 1$.

Both correction factors can be combined into a single correction factor.

$$\gamma = \alpha_{div}\alpha_i, \tag{2.14}$$

where γ is the total thrust correction factor (unitless). Equation 2.7 can now be rewritten as:

$$T = \gamma\sqrt{\frac{2m_i}{e}}I_b\sqrt{V_b}. \tag{2.15}$$

2.2.4 Specific Impulse for Electrostatic Ion Thrusters

Thrust efficiency is measured by specific impulse. Specific impulse is defined by the ratio of thrust to propellant mass flow rate.

$$I_{sp} = \frac{T}{\dot{m}_p g} \tag{2.16}$$

Substituting Equation 2.3 for thrust, equation 2.16 can be written as

$$I_{sp} = \frac{v_{ex}}{g}. \tag{2.17}$$

The mass utilization efficiency is the ratio of the ion mass flow rate to propellant mass flow rate.

$$\eta_m = \frac{\dot{m}_i}{\dot{m}_p} = \frac{I_b}{e}\frac{m_i}{\dot{m}_p} \tag{2.18}$$

Taking Equations 2.15 and 2.18, equation 2.16 becomes

$$I_{sp} = \frac{\gamma\eta_m}{g}\sqrt{\frac{2eV_b}{m_i}}. \tag{2.19}$$

Substituting $e = 1.602 \times 10^{-19}\,\mathrm{C}$ and $g = 9.807\,\mathrm{m/s^2}$ into Equation 2.19 yields,

$$I_{sp} = 1.417 \times 10^3 \gamma \eta_m \frac{\sqrt{V_b}}{\sqrt{m_a}} \qquad [\mathrm{s}]\,, \tag{2.20}$$

where m_a is the ion mass in amu.

The specific impulse for a thruster using argon propellant is

$$I_{sp} = 224.193 \gamma \eta_m \sqrt{V_b} \qquad [\mathrm{s}]\,. \tag{2.21}$$

Similarly for xenon, the specific impulse is

$$I_{sp} = 123.666 \gamma \eta_m \sqrt{V_b} \qquad [\mathrm{s}]\,. \tag{2.22}$$

The specific impulse for argon is plotted in Figure 2.9 against beam voltage and mass utilization efficiency assuming a thrust correction factor of 1. At a beam voltage of 1000 V, the theoretical peak specific impulse for 100 % mass utilization efficiency is 7090 s.

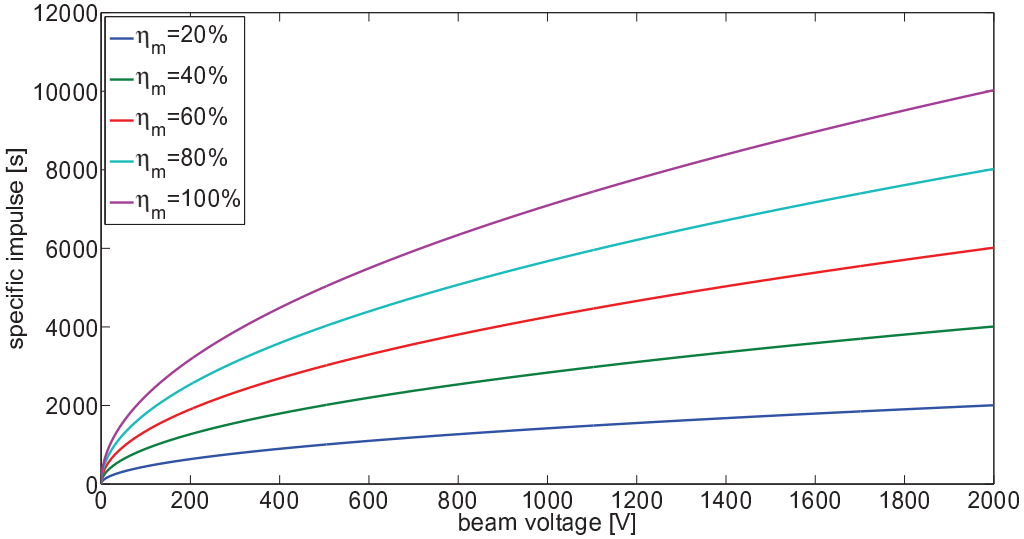

Figure 2.9: Specific impulse versus beam voltage for various mass utilization efficiencies for argon.

CHAPTER 3

THRUSTER DESIGN

The miniature ion thruster being analyzed consists of four main components: the ICP source, discharge chamber, ion optics, and neutralizer. The ICP source is a 1.5 cm planar spiral antenna fabricated in low temperature co-fired ceramic (LTCC). The discharge chamber is a cylinder, also fabricated in LTCC, with a diameter of 2 cm and a length of 3 cm. The ion optics consist of two electrostatic grids made of stainless steel. In this project, no neutralizer is currently being used. A cutaway drawing of the miniature ion thruster is shown in Figure 3.1.

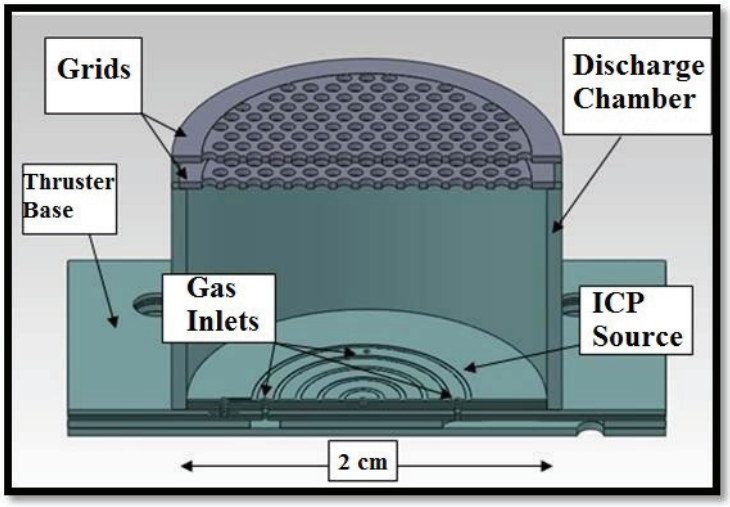

Figure 3.1: Cutaway drawing of the assembled miniature rf ICP source ion thruster.

3.0.5 ICP Antenna

LTCC has a relative permittivity of $\varepsilon_r = 7.8$ and a loss tangent of 0.006 at 3 GHz [39]. The ICP antenna in this thruster is a spiral planar antenna embedded in LTCC so it is not exposed to the plasma. Three ICP antennas were designed and studied using COMSOL Multiphysics [28, 29, 40]. Figure 3.2 is a photograph of the three ICP sources studied: α, β, and γ. Their dimensions are summarized in Table 3.1.

Figure 3.2: The three ICP antenna designs tested: α, β, and γ. The designs vary in diameter, pitch, and number of turns. [41]

Table 3.1: Dimensions of the three ICP sources

ICP Antenna	# of Turns	Diameter (mm)	Pitch (mm)
α	5	10.1	0.90
β	8	15	0.78
γ	5	15	1.45

Figure 3.3 shows an exploded view of the device and a magnified cross-section of one metal trace of the antenna. The fabrication process of these ICP sources are detailed in Reference [42].

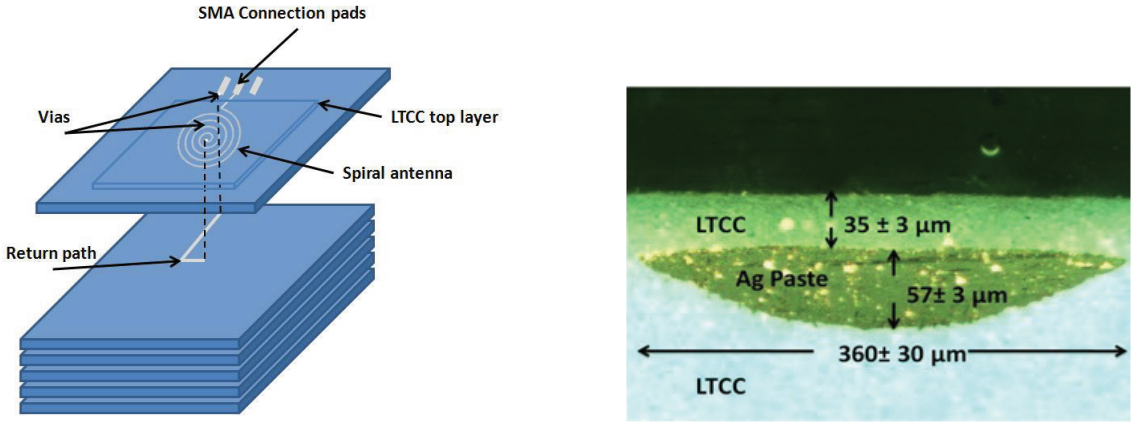

(a) (b)

Figure 3.3: (a) Exploded view of the ICP antenna showing the layers of LTCC, silver paste traces, vias, and SMA connection pads. (b) Photographed cross-section showing one turn of the ICP antenna between two layers of LTCC [42].

The COMSOL RF Module was used to simulate the electric field amplitude against frequency [28]. Three of these antennas were fabricated, and their electric field amplitudes were measured experimentally versus frequency. The measured results were then compared to the simulations, as shown in Figure 3.4 [28].

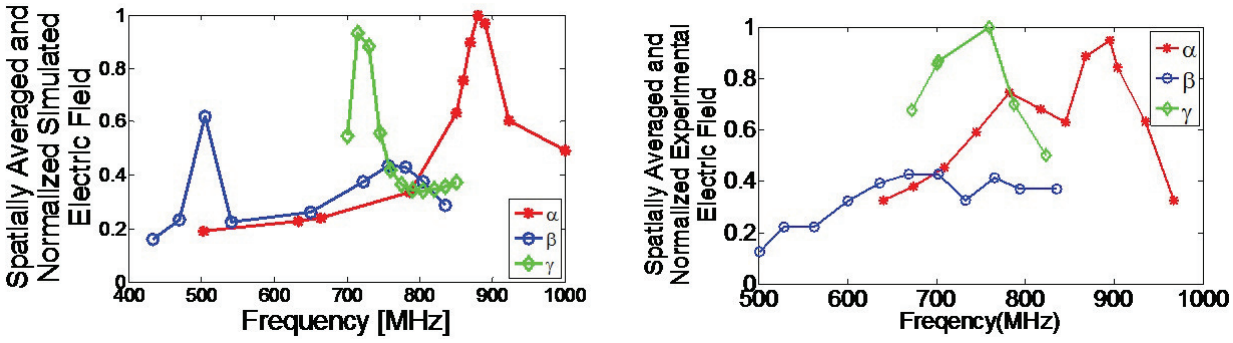

(a) (b)

Figure 3.4: (a) The plots of the spatially averaged normalized simulated electric field for ICP antennas α, β, and γ. I (b) The plots of the spatially averaged normalized measured electric field for ICP antennas α, β, and γ Christensen [28].

Each ICP source was tested for efficient plasma generation. The minimum amount

of rf power needed to strike a plasma was measured against frequency and pressure. The rf start power is shown in Figure 3.5. ICP source β was selected for thruster development because of consistent minimal rf start power over the frequency range $600 - 900\,\text{MHz}$.

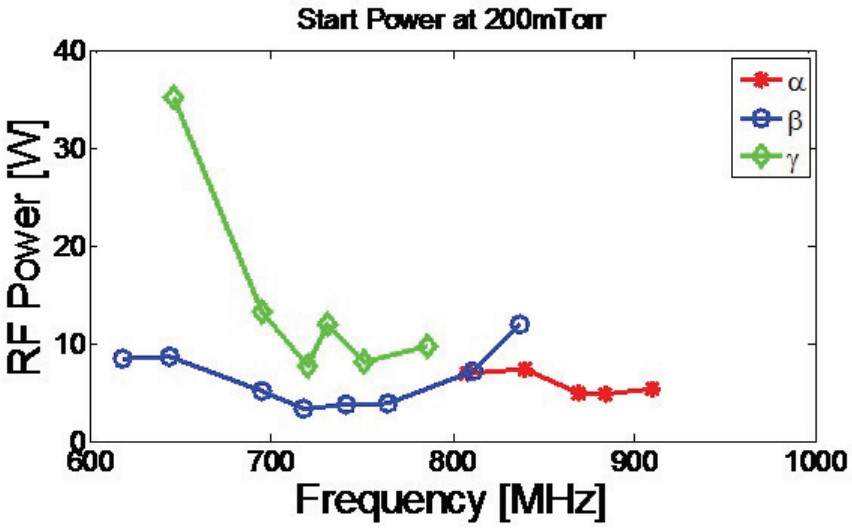

Figure 3.5: RF Start Power at 200 mTorr for ICP antennas α, β, and γ [41].

3.0.6 Discharge Chamber

The discharge chamber is an LTCC cylindrical tube. The fabrication process is outlined in Reference [43]. The tube initially had diameter of 2 cm and a length of 1.5 cm: a length-to-diameter ratio (L/D) of 0.75. These dimensions were initially selected because previous work found that a discharge chamber with a geometry of $L/D = 0.75$ had the best operating performance with a magnetic cusp [22]. Initial experimentation found that a longer tube was needed in order to keep the the electrostatic grid power supplies from saturating and not reaching full potential. The length of the discharge chamber was increased to 4.5 cm.

Magnetic cusps are used to increase the plasma density in the discharge chamber by confining electrons. Using the cyclotron frequency,

$$\omega_c = \frac{|q|\,B}{m_e}, \tag{3.1}$$

where ω_c is the cyclotron frequency (rad/s), B is the magnetic flux density (T), and m_e is the mass of an electron (kg), the Larmor radius can be found. The Larmor radius is the radius of a particle's orbit around magnetic field lines and is given by

$$r_c = \frac{v_\perp}{\omega_c}, \tag{3.2}$$

where r_c is the Larmor radius (m) and $v_\perp$ is the particle perpendicular velocity (m/s). Substituting Equation 3.1 into Equation 3.2, the Larmor radius can be rewritten as

$$r_c = \frac{v_\perp m_e}{|q|\,B}. \tag{3.3}$$

In order to increase plasma density, the applied magnetic field B must be large enough so that the Larmor radius $r_c \ll D$, the diameter of the thruster.

3.0.7 Ion Optics

The ion optics system uses two electrostatic stainless steel grids spaced closely together (0.5-2 mm). The grid closest to the plasma is known as the screen grid because it contains the plasma within the discharge chamber and screens the accelerator grid from high energy ion bombardment. The second grid is called the accelerator grid. The accelerator grid accelerates ions to high velocities, producing thrust. The ion optics are shown in Figure 3.6. This setup allows easy testing of various grid

configurations.

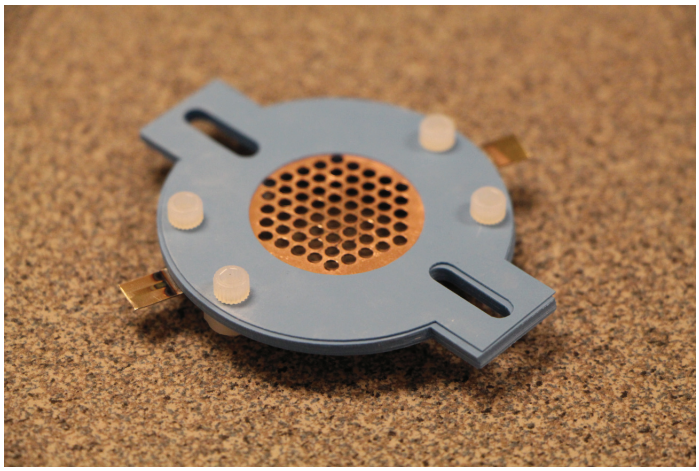

Figure 3.6: A photograph of the ion optics. Three pieces of LTCC are used to hold the grids together. This allows versatility in testing many different configurations of the ion optics such as the number of holes in the grids and separation distance between the grids.

3.0.8 Neutralizer

A neutralizer is needed in order to *complete the circuit*. As ions leave the thruster, the spacecraft becomes negatively charged. This charging will cause the ions to be attracted to the spacecraft, thus producing zero net thrust. To rectify this issue, a neutralizer is placed at the edge of the thruster near the accelerator grid. The neutralizer emits electrons into the ion plume. If done correctly, the ion plume will be neutralized. The electron emission is adjusted so that the electron current is equal to the ion current of the plume. In this work, a neutralizer was not needed because the experiments were conducted in a vacuum chamber with a grounded wall. In order to operate in space, the author acknowledges that a neutralizer will be needed for this design.

CHAPTER 4

EXPERIMENTAL SETUP AND METHODOLOGY

This experiment was set up to be controlled by a National Instruments LabVIEW virtual instrument (vi). This vi controls the rf, propellant delivery, and pressure control subsystems. The thruster throttle control system is controlled manually by hardware. Separate vi's control the Langmuir probe, ion collector plate, and the micronewton thrust measurement stand subsystems.

Electron temperature, plasma density, ion beam current, ion beam divergence angle, and thrust can be measured. Electron temperature and plasma density can be determined using the Langmuir probe system. Ion beam current, ion beam divergence angle, and thrust can be measured using the ion collector plate system. Thrust can also be measured using the micronewton thrust measurement stand.

4.0.9 Experiment Setup

The thruster main vi controls the rf, Propellant Delivery, and Pressure Control Subsystems. Communication in the control system is handled by the National Instruments PXI-1033 Chassis. The PXI-1033 houses a general purpose interface bus (GPIB) controller, which communicates with the signal generator and rf amplifier, and two PXI-6259 data acquisition (DAQ) cards for communication with all remaining digital and analog devices. The PXI-1033 is connected to the host PC via a PCI

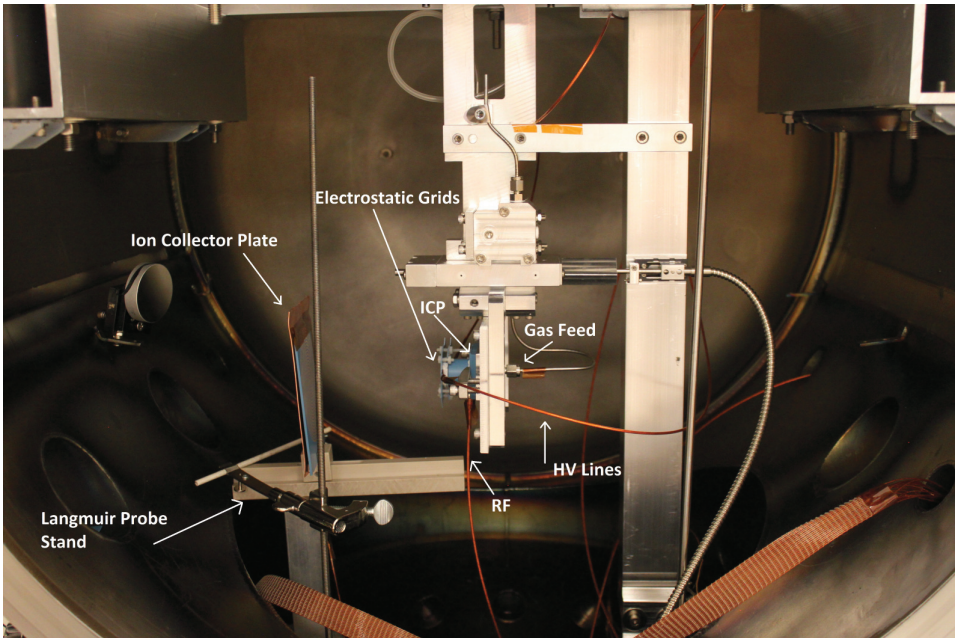

Figure 4.1: Vacuum Chamber Setup [41]

Express card.

The plasma source is biased slightly more positive than the screen grid in a typical ion thruster. This means that the ICP source would have to be referenced approximately to 1100 V. Doing this is quite difficult with laboratory equipment. In order to reduce this complication, the ICP source was referenced to ground in the experiments for this thesis. The screen grid was held at ground and the accelerator grid was biased at −1000 V. With this setup, the ions still gain the same energy as in the typical setup as in Figure 2.8. A schematic of the experimental setup of the ion thruster is shown in Figure 4.2.

RF System

RF power is delivered to the ICP antenna by the rf subsystem. A Hewlett-Packard E4420B signal generator outputs a sine wave into the input of an Empower 2021,

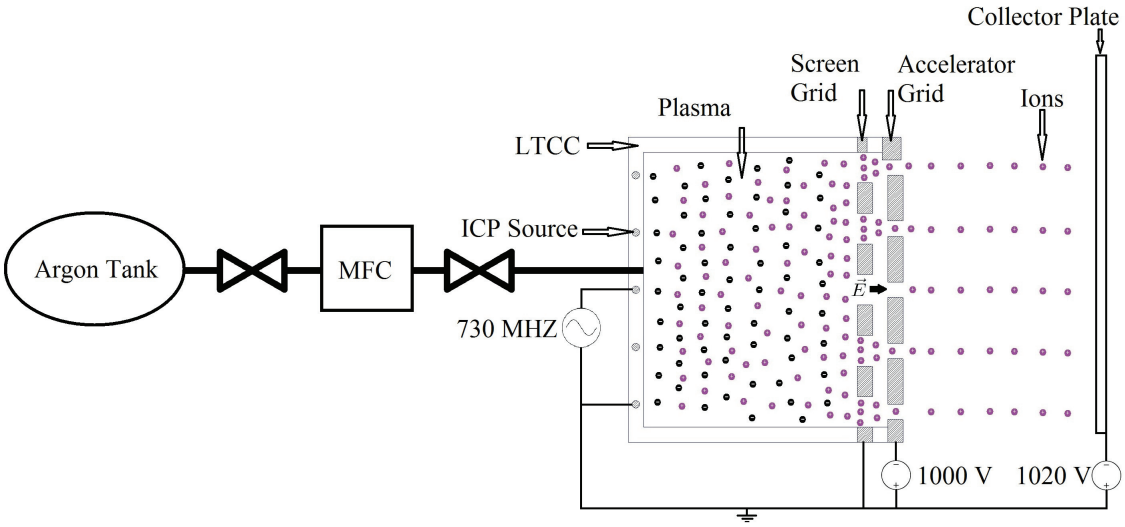

Figure 4.2: Experimental setup of the miniature ion thruster. The rf source is referenced to ground. The screen grid is held at ground while the accelerator grid is biased at $-1000\,\mathrm{V}$. A collector plate is used to measure the ion beam current. The collector is biased slightly more negative than the accelerator grid in order to prevent deceleration of ions.

50W broadband ($20 - 1000\,\mathrm{MHz}$) rf amplifier. The amplifier output is then fed into port 1 of an rf isolator. Port 3 of the isolator is a $50\,\Omega$ matched load that absorbs any reflected power to prevent damage to the rf amplifier. Port 2 is fed into a directional coupler. The coupler allows forward and reflected power to be measured. From the directional coupler, the signal is passed through a matching network consisting of variable capacitors. The matching network matches the ICP antenna as close to $50\,\Omega$ as possible to allow maximum forward and minimum reflected power. Matching is verified by using the the reflection measurement on a Hewlett-Packard 8712C 300 kHz-1300 MHz rf network analyzer. The output of the matching network then connects to an SMA feedthrough on the vacuum chamber. On the vacuum side of the chamber, a kapton insulated SMA cable is connected to the ICP antenna. A connection diagram of the RF Subsystem is shown in Figure 4.3.

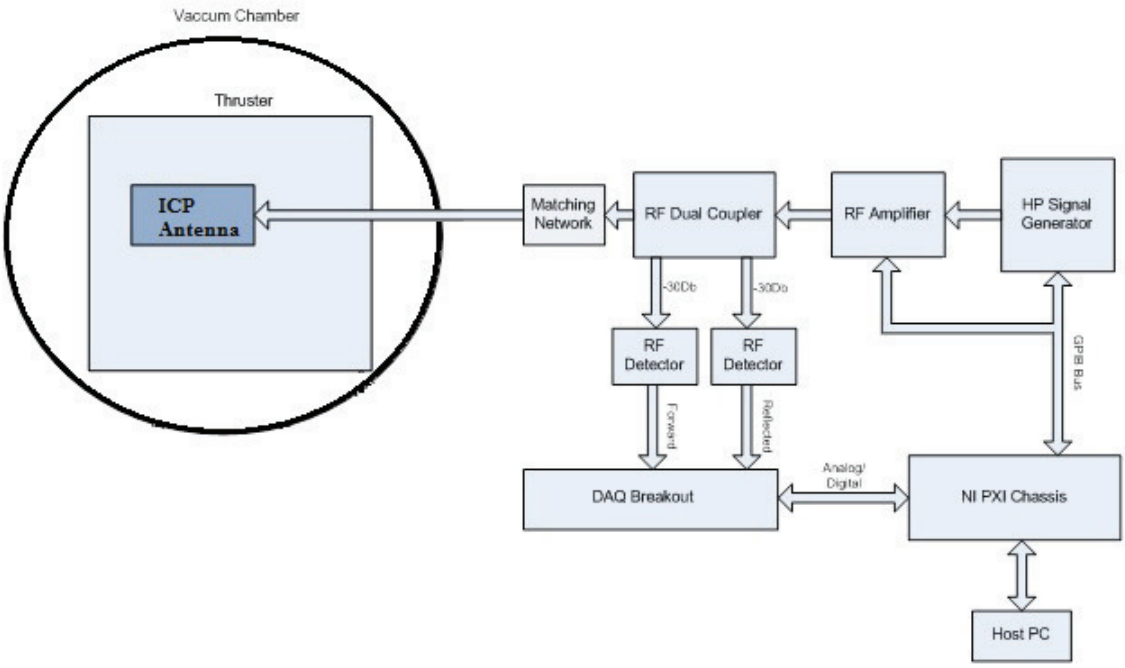

Figure 4.3: RF System Connection Diagram

Propellant Delivery System

The argon gas propellant is injected into the thruster using three different mass flow controllers (MFC) in parallel: a HORIBA STEC SEC-Z500, a Parker Porter Mass Flow Model 201, and another Parker Porter Mass Flow Model 201; referred to as the 4-sccm MFC, 28-sccm MFC, and 500-sccm MFC, respectively. The ranges of the MFCs are 0.08 sccm to 4 sccm, 0.05 sccm to 28 sccm, and 1 sccm to 500 sccm, respectively. This configuration allows for a broad range of gas flow rates during the experiment.

The 4-sccm MFC and 500-sccm MFC were already calibrated for argon gas from the manufacturer. However, the 28-sccm MFC feedback monitor needed to be corrected in the vi to show the true flow of argon gas, as given in Equation 4.1.

$$\dot{m}_{Ar} = 1.443\dot{m}_N, \tag{4.1}$$

where $\dot{m}_{Ar}$ is the mass flow rate of argon (sccm) and $\dot{m}_N$ is the mass flow rate of nitrogen (sccm).

Vacuum Test Chamber

The thruster experiments were conducted inside of a 75 cm long by 58 cm diameter cylindrical vacuum chamber. The chamber was previously part of a semiconductor processing sputtering device. Vacuum is achieved in the chamber by using a combination of a roughing pump and cryopump. After the chamber door has been sealed, a small valve is opened to the roughing pump, which brings the chamber from atmosphere to 100 Torr. At 100 Torr, a large valve is opened to the roughing pump allowing it to pump faster. This pump configuration brings the system down to 1 mTorr. At this point, both valves are closed, and the roughing pump is isolated from the chamber. The gate valve to the cryopump is opened via pneumatic valves. With the cryopump, the system can pulled down to 1×10^{-6} Torr, which is a suitable background pressure range to simulate low earth orbit.

There are three pressure gauges used to measure pressure in the system. There are two Kurt J. Lesker 275 series convection gauges and one InstruTech IGM400YFX Hornet Ion Gauge and Controller. The convection gauges are placed on opposite sides of the chamber with one gauge closer to the top and the other closer to the bottom. The vi displays the average of these two measurements on the front panel. Convection gauges are calibrated to measure pressure from 1×10^{-4} Torr to 1×10^{3} Torr. The ion gauge is effective for use from 1×10^{-9} to 5×10^{-2} Torr. The ion gauge turns on when the convection gauge reads 1×10^{-3} Torr.

The convection gauges are calibrated to the local atmospheric pressure at Boise State University, which sits at an altitude of 823 m [44]. The barometric formula (Equation 4.2) shows that the mean atmospheric pressure is 91821 Pa, or 688.716 Torr, at Boise State University.

$$\bar{p} = p_0 e^{-mgh/kT}, \tag{4.2}$$

where $\bar{p}$ is the mean atmospheric pressure at a given altitude above sea level (Pa), p_0 is the mean atmospheric pressure at sea level (101.325 kPa), g is acceleration due to gravity (9.807 m/s^2), m is the mass of the molecule (kg), h is altitude above sea level (m), k is the Boltzmann constant (1.38×10^{-23} J/K), and T is the mean temperature (K).

Since the experiments are performed with argon gas, the convection gauges were calibrated according the curve in Figure 4.4 [45]. The ion gauge correction factor for argon is 1.29 [45]. A correction curve is produced in Figure 4.4 from Equation 4.3.

$$p_{Ar} = \frac{p_g}{1.29} \tag{4.3}$$

where p_{Ar} is the argon pressure (Torr) and p_g is gauge pressure (Torr).

Thruster Throttle Control System

The thruster control subsystem consists primarily of two DC-to-DC converters for the electrostatic grids. The screen grid is biased positive with respect to ground using an UltraVolt 2D15-P2 DC-to-DC converter. The output is varied from 0 to 2000 V by a 0 V to 5 V control signal from a 1 MΩ potentiometer. An UltraVolt 1D15-N1 is used to bias the accelerator grid negative from 0 V to −1000 V in the same manner as the screen grid. Both DC-to-DC converters have voltage and current monitor signals that

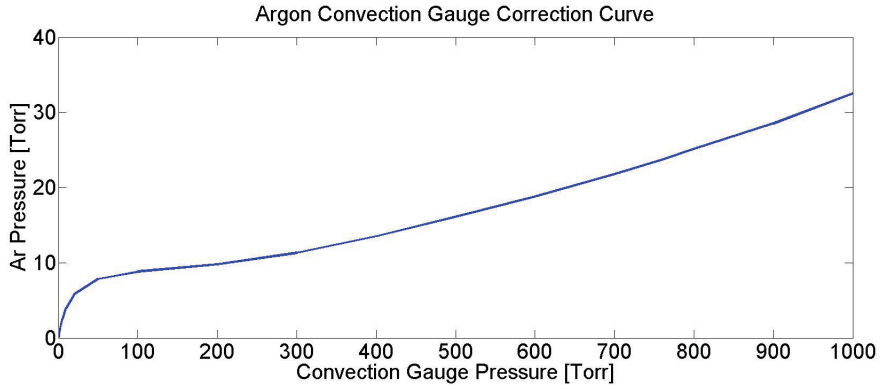

(a)

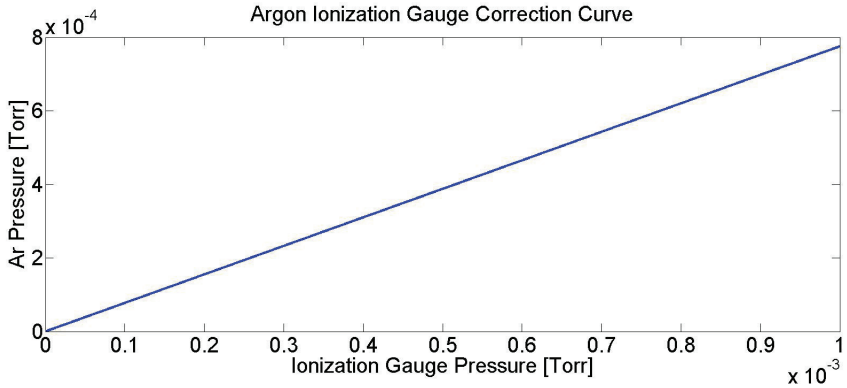

(b)

Figure 4.4: (a) The argon gas correction curve for the convection gauge. (b) The argon gas correction curve for the ion gauge .

are output to four LCD voltmeter displays. The high voltage signal is delivered to the chamber via a 10-pin HV vacuum flange. From the flange, HV is delivered to the grids by two kapton-coated vacuum coaxial cables (coax). Coax was used in order to use the built-in woven copper shield as a ground shield to prevent the inner copper core (which is carrying the HV) from discharging and creating undesired plasma during tests at high pressure ($> 1 \times 10^{-3}$ Torr).

(a)

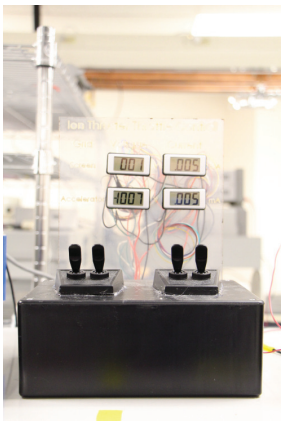

(b)

Figure 4.5: (a) The throttle control circuit housing is shown. Two 1 MΩ potentiometers are used to control voltages applied to the screen and accelerator grids. (b) The throttle control feedback monitor is shown. The monitor is made of four LCD voltmeters that display the voltage and current drawn from each HV DC-to-DC converter.

Langmuir Probe System

A Langmuir probe is used to measure the ICP electron temperature and plasma density. The measurement circuit is shown in Figure 4.6. The probe is a length of kapton wire insulated by a ceramic tube. At one end of the tube, a small area of conductor is exposed.

To measure the plasma density and the electron temperature, the probe bias is swept from −50 V to+50 V. During the sweep, the probe current is measured across a 500 Ω resistor. This data produces a current-voltage (I-V) characteristic curve. From this I-V curve, electron temperature and plasma density can be calculated. This calculation will be discussed in detail in Section 5.1.

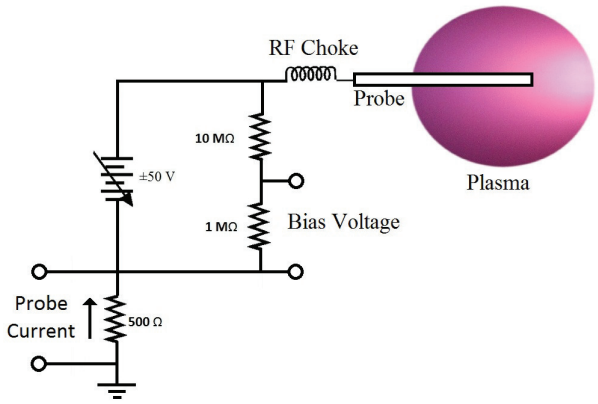

Figure 4.6: A cylindrical probe is swept from −50 V to 50 V. An rf choke is placed in series to filter out rf noise from the plasma. The bias voltage was measured by means of a voltage divider that allows a −5 V to 5 V input to LabVIEW. The probe current was found by measuring the voltage across the 500 Ω resistor and then dividing the voltage by the resistance of the resistor.

Ion Collector Plate System

Two different ion collector plates were used in this experiment: a single pad and a radial segmented ion collector. The single pad ion collector plate is a 100 mm by 150 mm copper plate used to measure the total ion beam current exiting the thruster. The radial segmented ion collector was used to map the geometry of the ion beam. The radial pad consists of 5 concentric rings of varying radii to measure the divergence of the beam.

The silver paste used to make the pads was easily sputtered by the ion beam during the initial use of the 19-pad segmented collector. A backup radial segmented collector was made using five concentric copper circles of varying radii: 50 mm, 40 mm, 30 mm, 20 mm, and 10 mm. Wire connections were made by using vacuum compatible conductive tape and the layers were insulated using Kapton tape.

In order to take accurate ion beam current measurements, the collectors must be at the same potential of the ion beam. Since typical DAQ systems do not allow floating

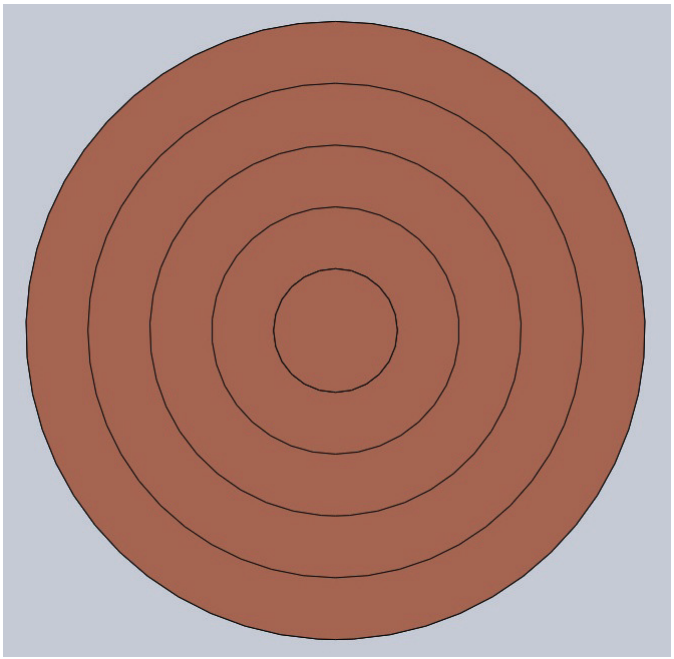

Figure 4.7: CAD drawing of the five-segmented radial collector. The innermost collector has a radius of 10 mm and the outermost segment has a radius of 50 mm.

measurements of several hundred volts, a special conversion circuit was needed. Five four-channel opto-isolator boards were used to accomplish this. This gave a total of twenty channels, enough for all 19 pads for each collector plate. A photograph of one of the opto-isolator boards is shown in Figure 4.8.

4.1 Experimental Procedure

Table 4.1 contains a summary of the experiments performed in this research. The ICP source was characterized in a series of three experiments (1A, 1B, and 1C). A Langmuir probe was used to measure the plasma density while varying the rf input power supplied to the ICP source and the propellant mass flow rate. The density was measured at 1, 2.5, 5, 10, 20, and 25 W of rf power for propellant mass flow rates of 0.1, 1, 2.5, 5, and 10 sccm. The measurement was performed three times for each of

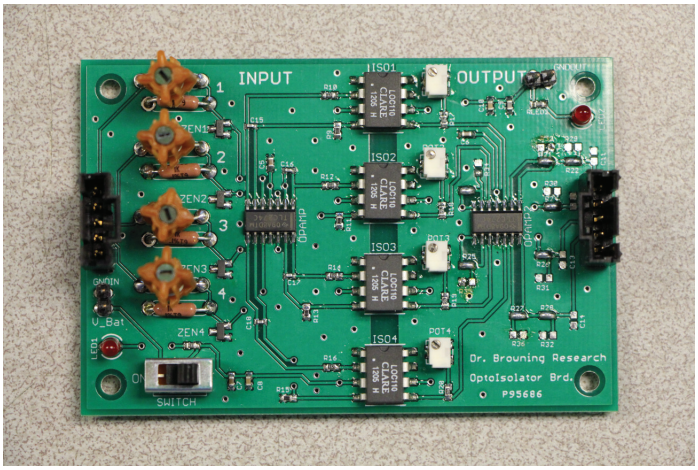

Figure 4.8: Photograph of an opto-isolator board. There are four input and output channels. The ground for the input channels on the left side of the board floats to −1000 V. The ion beam current is measured by measuring the voltage across a high precision (0.1%) 1 kΩ resistor. A series high frequency inductor used an rf choke to filter out interference from the ICP source. The output channels on the right side of the board are referenced to earth ground so the signals can be safely read by a DAQ system.

the 25 scenarios. Experiment 1A measured the plasma density with the ICP source by itself. The discharge chamber was added to the ICP source for Experiment 1B. Finally, a magnetic cusp was added to the ICP source and discharge chamber for Experiment 1C.

Thrust was measured at various levels of rf power (1, 2.5, 5, 10, 20, and 25 W) and propellant flow rates at three different frequencies: 710, 730, and 750 MHz (Experiments 2A, 2B, and 2C, respectively). Ion beam current was measured using the single pad collector plate.

In Experiment 3A, the radial ion collector plate was used to determine the ion beam divergence for the optimum cases determined by Experiment 2. Using the results of Experiments 2 and 3, the total thrust, specific impulse, mass utilization efficiency, electrical efficiency, and the total efficiency can be calculated.

Table 4.1: Summary of Experiments

Experiment	Description
1A	Measure plasma density with ICP source only
1B	Measure plasma density with ICP source and discharge chamber
1C	Measure plasma density with ICP source, discharge chamber, and magnetic cusp system
2A	Measure thrust at 710 MHz
2B	Measure thrust at 730 MHz
2C	Measure thrust at 750 MHz
3A	Measure the ion beam divergence at the optimum condition

CHAPTER 5

RESULTS AND DISCUSSION

In this chapter, the results of experiments are given. A photograph of the thruster operating is shown in Figure 5.1. The ICP source is on the right side of the photograph and an ion collector plate is shown on the left side. Individual ion beamlets can be seen exiting the holes in the electrostatic grids and then impacting the ion collector plate. The thruster is operating at a frequency of 730 MHz with 5 W of rf power and 5 sccm of argon mass flow.

In Section 5.1, the Langmuir probe data is extensively detailed. In Section 5.2, the thrust measurements from the ion collector plates are investigated. Finally, in Section 5.3, the mass and electrical efficiencies of the miniature ion thruster are calculated.

5.1 Langmuir Probe Analysis and ICP Source Characterization Results

The IV-curve from a Langmuir probe can be used to extract characteristics of a plasma such as the electron temperature and the ion density. For this study, a method outlined by Reference [46] was used. Using a cylindrical wire probe, the measured current is

$$I = 2en_s ad\sqrt{\frac{2e\left|\Phi_p - V_B\right|}{m_i}}, \tag{5.1}$$

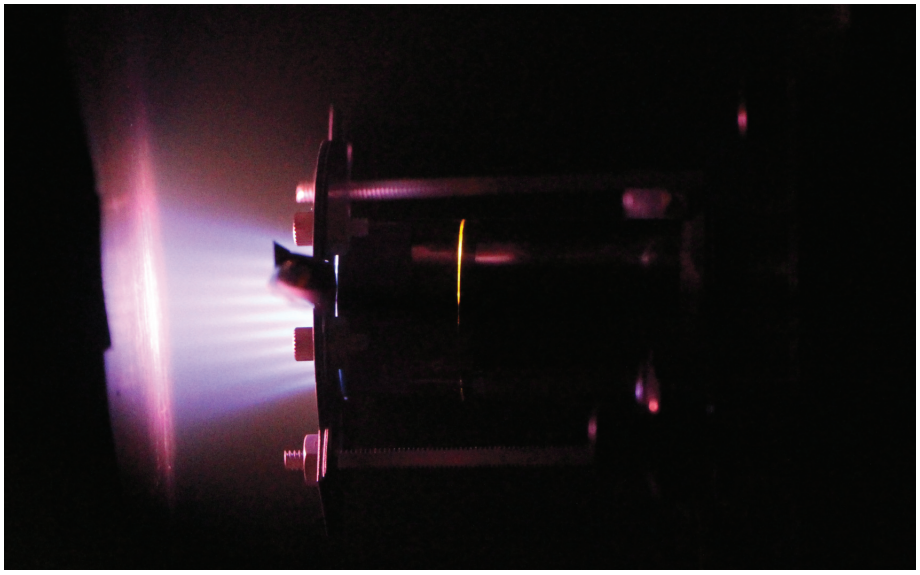

Figure 5.1: Photograph of the miniature rf ICP source ion thruster operating. On the left side of the photograph, an ion collector plate was placed down stream of the thruster in order to measure ion beam current. Individual ion beamlets can be seen exiting the thruster. The thruster is operating at a frequency of 730 MHz with 5 W of rf power and 5 sccm of argon mass flow.

where n_s is the sheath edge plasma density (m^{-3}), a is the probe radius (m), d is the probe length (m), m_i is the ion mass (kg), V_B is the probe bias voltage (V), and Φ_p is the plasma potential (V). The probe used in these experiments had a radius of 0.30 mm and a length of 2.27 mm. Squaring Equation 5.1 and solving for n_s yields

$$n_s = \frac{1}{2ead\sqrt{\frac{2e}{m_i}}}\sqrt{\frac{I^2}{|\Phi_p - V_B|}} \tag{5.2}$$

where the $\frac{I^2}{|\Phi_p - V_B|}$ term is the slope of IV-curve in the ion saturation region. The sheath plasma density is related to the bulk plasma density by the approximation

$$n_0 \approx \frac{n_s}{0.61} \tag{5.3}$$

where n_0 is the bulk plasma density (m^{-3}). Substituting Equation 5.3 into Equation 5.2 yields.

$$n_0 \approx \frac{1}{2ead\,(0.61)\sqrt{\frac{2e}{m_i}}}\sqrt{\frac{I^2}{|\Phi_p - V_B|}} \tag{5.4}$$

Electron current saturation was not reached during the Langmuir probe experiments; therefore the electron temperature could not be calculated. The I-V characteristic curves for Experiments 1A and 1B are shown in Figures 5.2 and 5.3, respectively. For Experiment 1A, the maximum probe current in the ion saturation region is 300 μA when the ICP source was operating at 25 W of rf power at 730 MHz at an argon mass flow rate of 10 sccm. The maximum probe current for Experiment 2A in the ion saturation region is 700 μA with the ICP source operating at the same conditions previously stated.

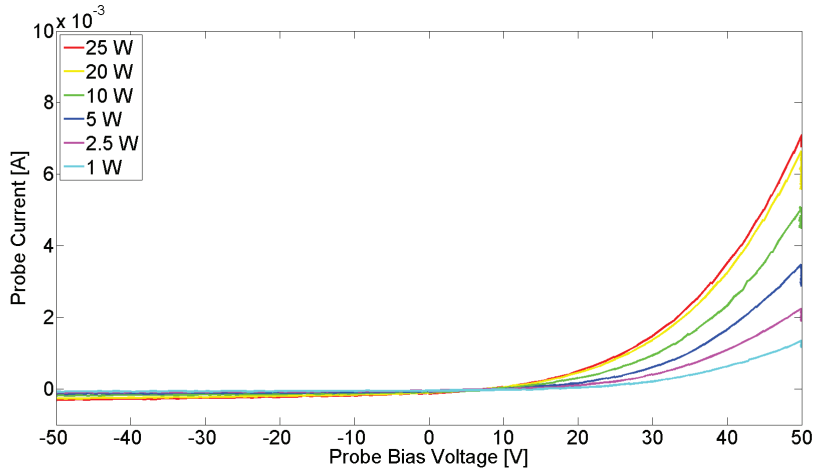

Figure 5.2: Experiment 1A (ICP source only) I-V Characteristic for 10 sccm Ar gas flow rate for various rf powers at 730 MHz.

Using Equation 5.4, the plasma density for Experiments 1A and 1B were plotted in Figures 5.4 and 5.5, respectively. As expected, the greatest plasma densities were achieved with higher propellant mass flow rates at high rf power. The greatest density

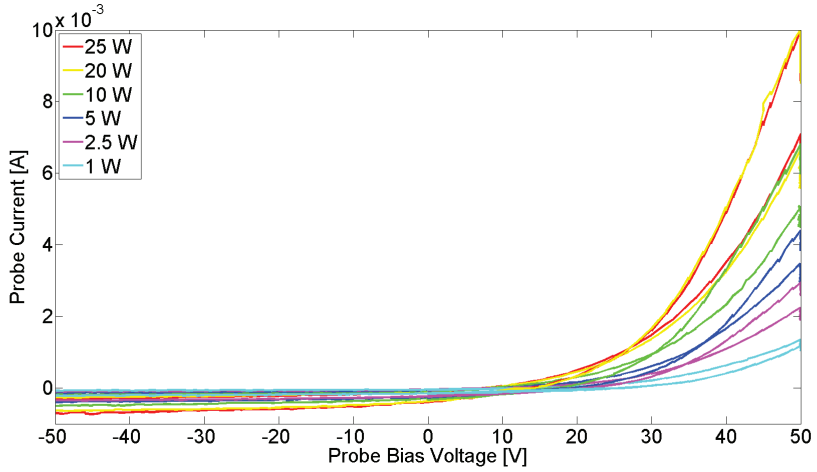

Figure 5.3: Experiment 1B (ICP source and discharge chamber) I-V characteristic for 10 sccm Ar gas flow rate for various rf powers at 730 MHz.

achieved for the solo ICP source was $1.1 \times 10^{18}\,\mathrm{m}^{-3}$ at an argon mass flow rate of 10 sccm and an rf power of 25 W. The greatest density achieved for the ICP source with the discharge chamber was $2.75 \times 10^{18}\,\mathrm{m}^{-3}$ at an Ar mass flow rate of 10 sccm and an rf power of 25 W. Results from Experiment 1C are not shown. The magnetic cusp system did not show a noticeable improvement of plasma density to that of Experiment 1B. Stronger permanent radial magnets are needed for better electron confinement. The addition of the discharge chamber showed an increase of $132 - 385\,\%$.

5.2 Thrust Measurements Results

5.2.1 Single Pad Collector Plate

The ion current produced by the thruster was measured using the single pad collector plate connected to the opto-isolator circuit. The current was measured at three different frequencies: 710 MHz, 730 MHz, and 750 MHz. For each frequency, ion

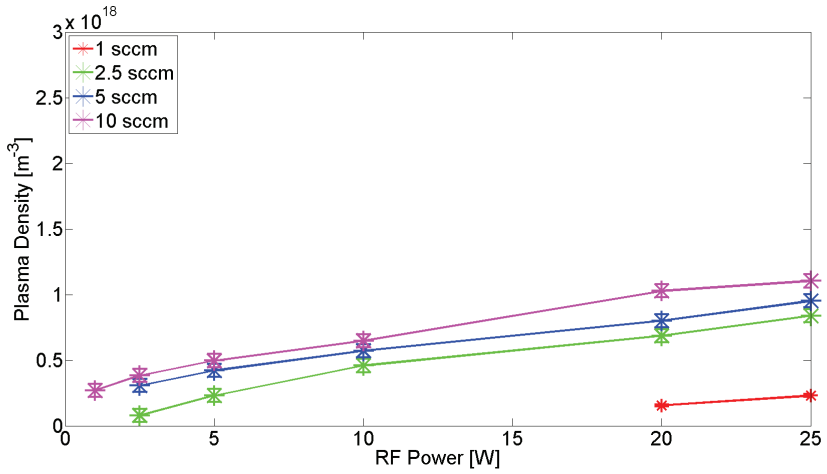

Figure 5.4: Experiment 1A (ICP source only) results showing plasma density versus rf power for various gas flow rates at 730 MHz. [41]

current was measured at six rf power levels at four propellant mass flow rates. These measurements were conducted at two electrostatic grid separations: $d = 0.42$ mm and $d = 2.02$ mm. Using Equation 2.8, the thrust were calculated for these measurements and the results are shown in Figures 5.6-5.11.

In order to determine an optimum operating condition for the thruster, a figure of merit was developed.

$$\chi = \frac{I_b}{I_{total}} = \frac{I_b}{I_s + I_a + I_b} \tag{5.5}$$

where χ is a figure of merit ($0 \leq \chi \leq 1$), I_{total} is the total current (A), I_s is the current drawn by the screen grid, and I_a is the current drawn by the accelerator grid. The greatest value of χ will determine the optimum operating condition. χ is shown for the whole data set in subfigure (b) of Figures 5.6-5.11. The highest figure of merit ($\chi = 0.85$) occurred while the ICP source was operating at 5 W at 730 MHz with a 5 sccm propellant flow rate and a grid separation distance of 0.42 mm (Figure 5.7).

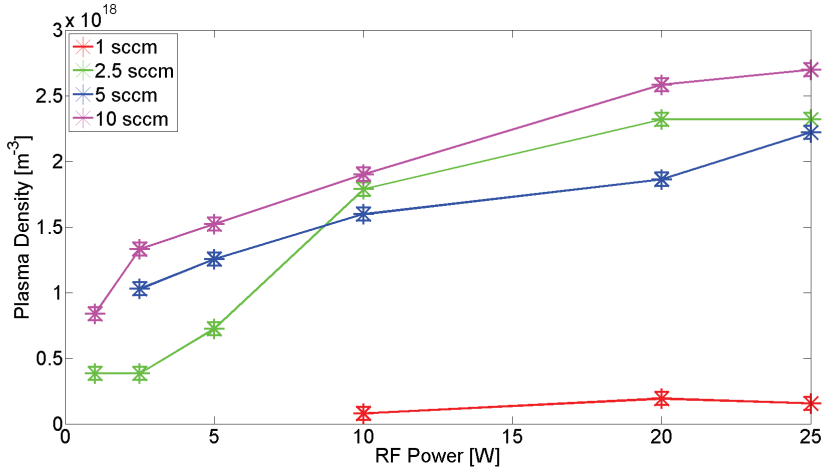

Figure 5.5: Experiment 1B (ICP source and discharge chamber) results showing plasma density versus rf power for various gas flow rates at 730 MHz. [47]

The ion beam divergence was calculated at this operating condition. χ generally did not improve as the rf power was increased. This is because the plasma reaches a saturation point when increasing rf power no longer aides in ion production. The highest value of χ for each frequency are summarized in Table 5.1. The greatest ideal thrust occurred when the thruster was operating at 750 MHz with 10 W of rf power, however its figure of merit was only 0.57, which would later translate to a much lower electrical efficiency.

Frequency [MHz]	d [mm]	χ	T [μN]	$\dot{m}_p$ [sccm]	P_{rf} [5]
710	0.42	0.84	24.34	5	5
710	2.02	0.70	21.16	10	5
730	0.42	0.85	24.92	5	5
730	2.02	0.64	19.12	5	10
750	0.42	0.79	26.09	5	10
750	2.02	0.57	25.20	5	10

Table 5.1: Highest values of χ for each frequency in Experiment 2

It is important to note that at the point in time that these experiments were

conducted, the ICP source was unable to initiate and sustain a plasma for argon mass flow rates less than 5 sccm. Performance degradation of the device was most likely due to a build up of sputtered material on the inside of the discharge chamber and on the surface of the ICP source from the electrostatic grids and collector plates.

5.2.2 Ion Beam Divergence

The current density, as seen in Figure 5.12, was measured at the optimum operating condition for various beam voltages. For $V_b = 1000\,\mathrm{V}$, the current density is maximum at $0\,\mathrm{mm} < r < 10\,\mathrm{mm}$ with $1.2\,\mathrm{A/m^2}$. At $40\,\mathrm{mm} < r < 50\,\mathrm{mm}$, the current density has decreased to $35.4\,\mathrm{mA/m^2}$.

Figure 5.13 shows the cumulative percentage of total ion current density versus radial position. This means, for $V_b = 1000\,\mathrm{V}$, 58.92 % of the total beam current density is located within the range of $0\,\mathrm{mm} < r < 10\,\mathrm{mm}$, 83.47 % of the total beam current density is within the range of $0\,\mathrm{mm} < r < 20\,\mathrm{mm}$, etc. The segmented collector was placed 35 mm downstream of the thruster. Using Equation 2.12, the thrust correction factor $\alpha_{div} = 0.90$. Taking the inverse cosine of this correction factor gives a beam divergence angle of 26.25°.

5.3 Efficiency

5.3.1 Mass Utilization Efficiency

Mass utilization efficiency is an important measure of an ion thruster performance. High mass utilization efficiency indicates a high fraction of ionization. It is calculated by dividing the mass flow of ions by the mass flow of propellant.

$$\eta_m = \frac{\dot{m}_i}{\dot{m}_p} = \frac{I_b}{e}\frac{m_i}{\dot{m}_p}, \tag{5.6}$$

where η_m is the mass utilization efficiency.

The mass flow of ions is found by multiplying the beam current by the mass of the ion and then dividing by the charge of the ion. The current has units of amperes, which is equivalent to coulombs per second. When multiplied by the ion mass in kilograms and then dividing by the charge in coulombs, this result produces an ion mass flow rate with units of kilograms per second. Equation 5.7 shows the conversion from sccm to kg/s [48].

$$1\,\text{sccm} = 2.973 \times 10^{-8}\,\text{kg/s}, \tag{5.7}$$

Table 5.2: Argon Flow Conversion Table [48]

sccm	kg/s
10	2.973×10^{-7}
5	1.487×10^{-7}
2.5	7.433×10^{-8}
1	2.973×10^{-8}
0.1	2.973×10^{-9}

For the optimum operating condition, the propellant mass flow rate was 5 sccm and the ion beam current was 0.86 mA. Plugging in $e = 1.602 \times 10^{-19}\,\text{C}$, $m_i = 6.68179 \times 10^{-26}\,\text{kg}$, and $\dot{m}_p = 1.487 \times 10^{-7}\,\text{kg/s}$ into Equation 5.6 yields a mass utilization efficiency of 0.24 %.

5.3.2 Electrical Efficiency

The electrical efficiency of an ion thruster is calculated by dividing the output power of the thruster (i.e., the beam current multiplied by the net ion acceleration voltage) by the total input power. The total input power includes the rf power supplied to the ICP antenna and the power the ion optics draw from the high voltage supplies.

$$\eta_e = \frac{P_{out}}{P_{in}} = \frac{P_b}{P_{rf} + P_{IO}}, \tag{5.8}$$

where η_e is the electrical efficiency, P_{out} is the total output power, P_{in} is the total input power (W), P_b is the beam power (W), P_{rf} is the input rf power (W), and P_{IO} is the power supplied to the ion optics (W). For the optimum operating condition, $P_{rf} = 5\,\mathrm{W}$, $V_b = 1000\,\mathrm{V}$, $I_b = 0.86\,\mathrm{mA}$, $I_a = 0.076\,\mathrm{mA}$, $V_a = -1000\,\mathrm{V}$. Plugging these values into Equation 5.8 yields an electrical efficiency of 16.94 %.

Ion production efficiency is the electrical cost to produce ions. It is found by dividing the total power to produce ions by the beam current [36].

$$\varepsilon_B = \frac{P_{in}}{I_b}, \tag{5.9}$$

where ε_B is electron-ion pair energy cost (W/A = eV/ion). For the optimum operating condition, $\varepsilon_B = 5.9\,\mathrm{keV/ion}$.

5.3.3 Total Efficiency

The total efficiency of the thruster is found by dividing the kinetic thrust power of the thruster by the total input power. Kinetic thrust power is also known as jet power. The jet power is the kinetic energy of the exhaust particles [36].

$$P_{jet} = \frac{1}{2}\dot{m}_p v_{ex}^2, \tag{5.10}$$

where P_{jet} is the jet power (W). Using equation 2.3, the jet power can be rewritten as,

$$P_{jet} = \frac{T^2}{2\dot{m}_p}, \tag{5.11}$$

and the total efficiency can now be described as:

$$\eta_{_T} = \frac{P_{jet}}{P_{in}} = \frac{T^2}{2\dot{m}_p P_{in}}, \tag{5.12}$$

where $\eta_{_T}$ is the total efficiency. Substituting thrust from Equation 2.15 into Equation 5.12 yields:

$$\eta_{_T} = \gamma^2 \frac{I_b m_i}{e\dot{m}_p} \frac{I_b V_b}{P_{in}} = \gamma^2 \eta_m \frac{I_b V_b}{P_{in}}. \tag{5.13}$$

Finally, solving Equation 5.8 for P_{in} and then substituting into Equation 5.13 yields,

$$\eta_{_T} = \gamma^2 \eta_m \eta_e. \tag{5.14}$$

Using $\alpha_i = 1$ and $\gamma = 0.9$, $\eta_m = 0.24\,\%$, and $\eta_e = 16.94\,\%$, the total efficiency of the thruster is $0.033\,\%$. This value is far too small (a factor of 1000) for practical use.

5.3.4 Thrust and Specific Impulse

When using argon as a propellant, the equation for thrust is

$$T = 913.285\gamma I_b \sqrt{V_b} \qquad [\mu\text{N}].$$

Using the values for the optimum operating condition, the thrust produced by the thruster is 22.35 μN.

The equation for specific impulse with argon propellant is

$$I_{sp} = 224.193\gamma\eta_m\sqrt{V_b} \qquad [\text{s}]\,.$$

Using the values for the optimum operating condition, the specific impulse of the thruster is 15.31 s. Results are summarized in Table 5.3.

Table 5.3: Summary of Results

Parameter	Value
P_{rf}	5 W
$\dot{m}_p$	5 sccm
V_s	0 V
I_s	0.075 mA
V_a	−1000 V
I_a	0.076 mA
V_b	1000 V
I_b	0.86 mA
θ	26.25°
α_{div}	0.90
α_i	1
γ	0.90
η_m	0.24 %
η_e	16.94 %
ε_B	5.9 keV/ion
η_T	0.033 %
T	22.35 μN
I_{sp}	15.31 s

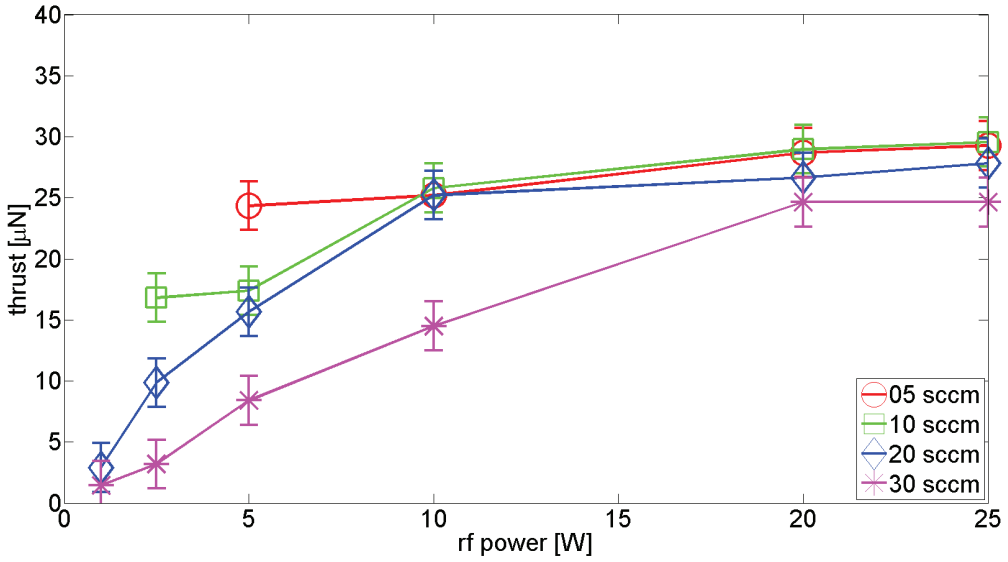

(a)

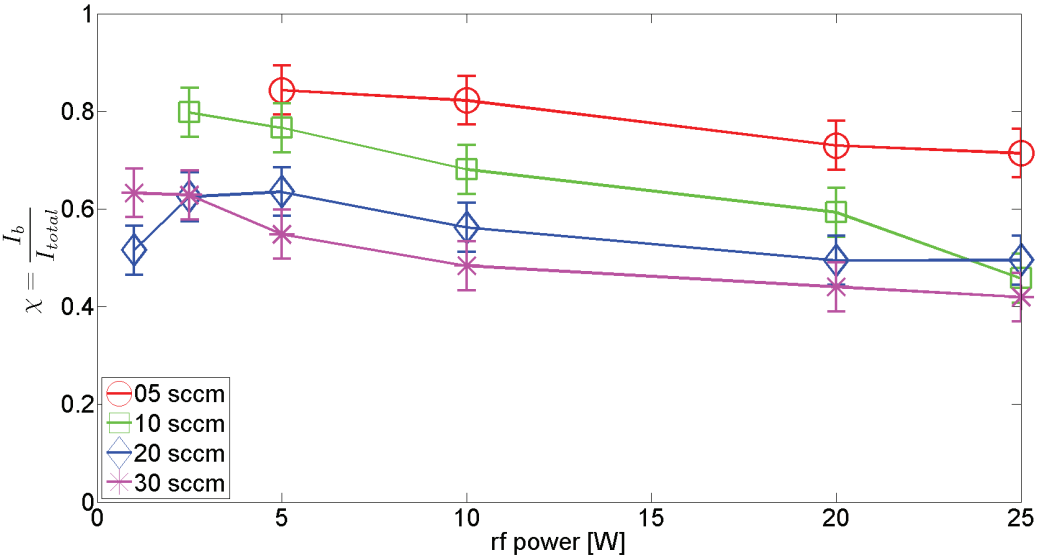

(b)

Figure 5.6: (a) Ideal thrust was calculated for various propellant mass flow rates and rf power levels from ion beam current with the ICP source operating at 710 MHz and an electrostatic grid separation of $d = 0.42$ mm. (b) A figure of merit was calculated for various propellant mass flow rates and rf power levels from the measured ion beam current and grid currents with the ICP source operating at 710 MHz and an electrostatic grid separation of $d = 0.42$ mm.

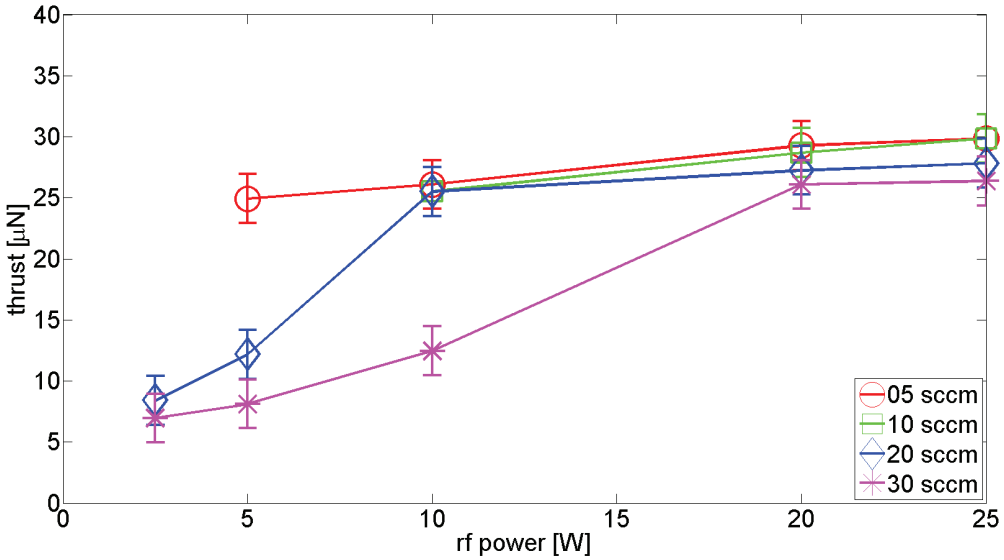

(a)

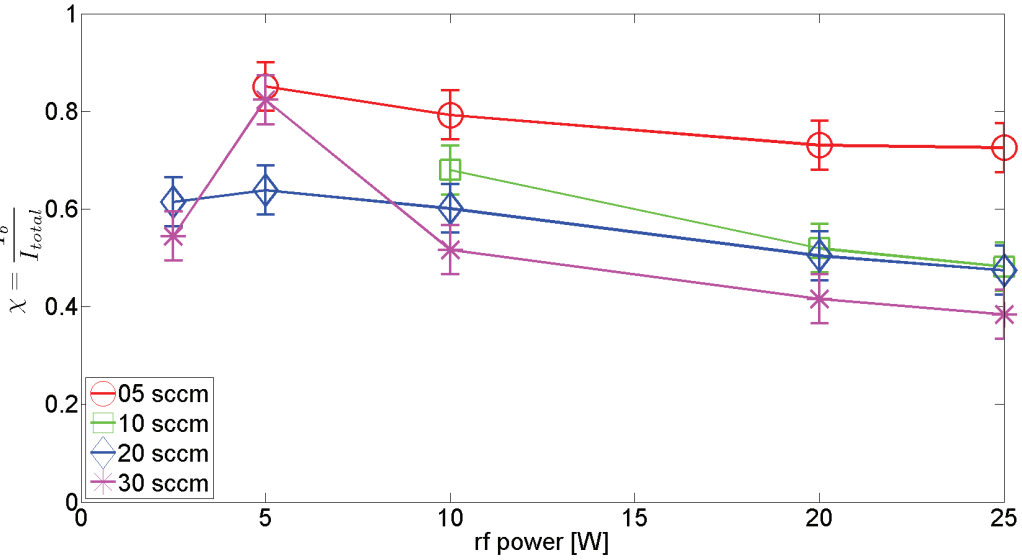

(b)

Figure 5.7: (a) Ideal thrust was calculated for various propellant mass flow rates and rf power levels from ion beam current with the ICP source operating at 730 MHz and an electrostatic grid separation of $d = 0.42$ mm. (b) A figure of merit was calculated for various propellant mass flow rates and rf power levels from the measured ion beam current and grid currents with the ICP source operating at 730 MHz and an electrostatic grid separation of $d = 0.42$ mm.

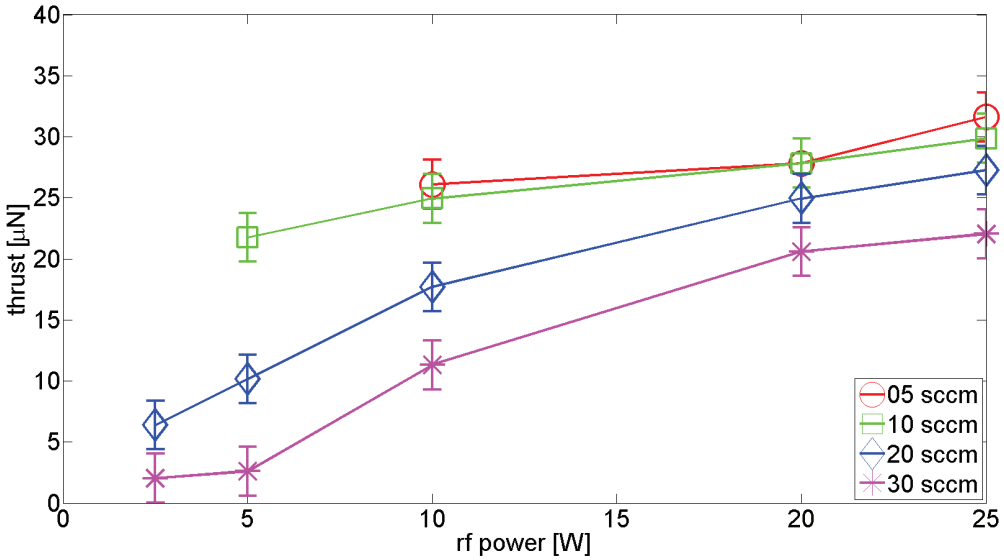

(a)

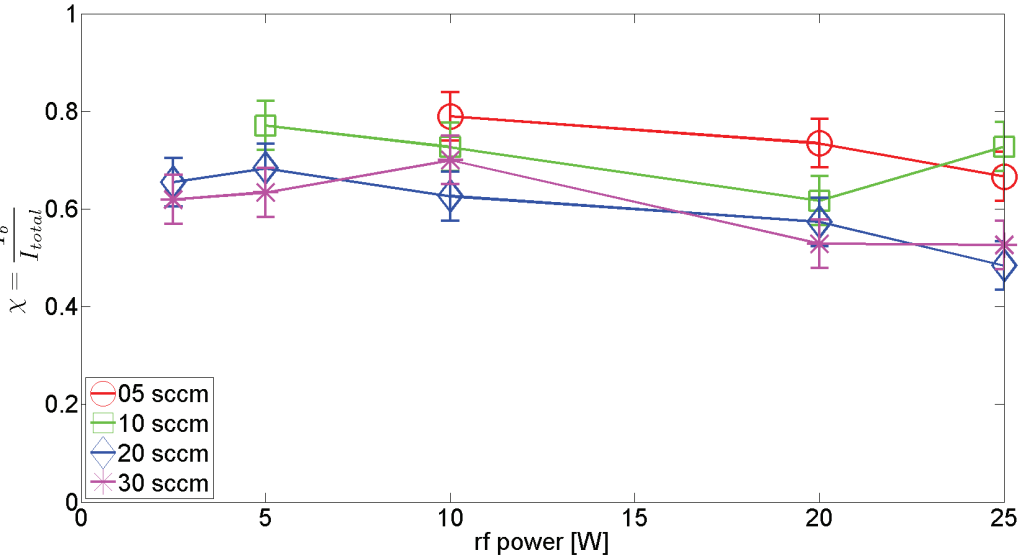

(b)

Figure 5.8: (a) Ideal thrust was calculated for various propellant mass flow rates and rf power levels from ion beam current with the ICP source operating at 750 MHz and an electrostatic grid separation of $d = 0.42$ mm. (b) A figure of merit was calculated for various propellant mass flow rates and rf power levels from the measured ion beam current and grid currents with the ICP source operating at 750 MHz and an electrostatic grid separation of $d = 0.42$ mm.

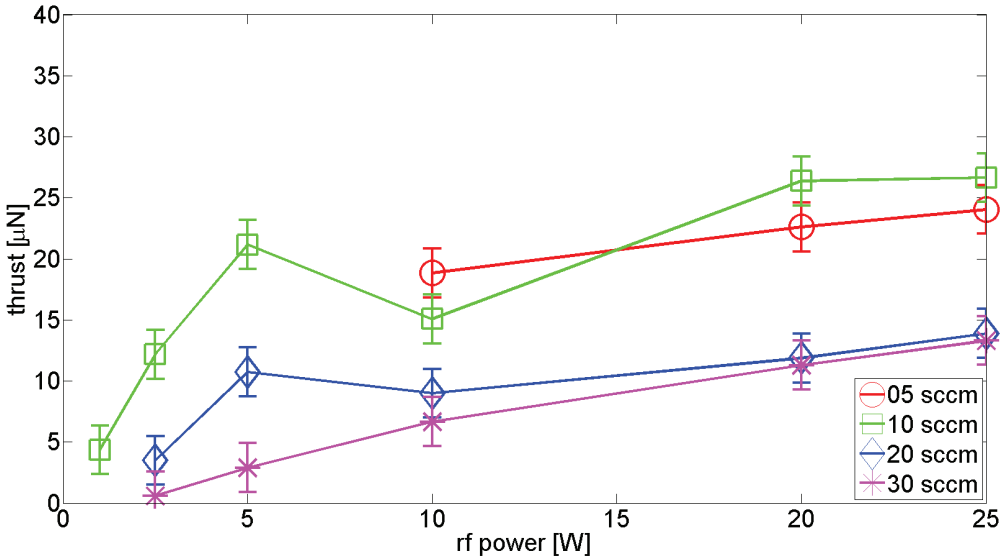

(a)

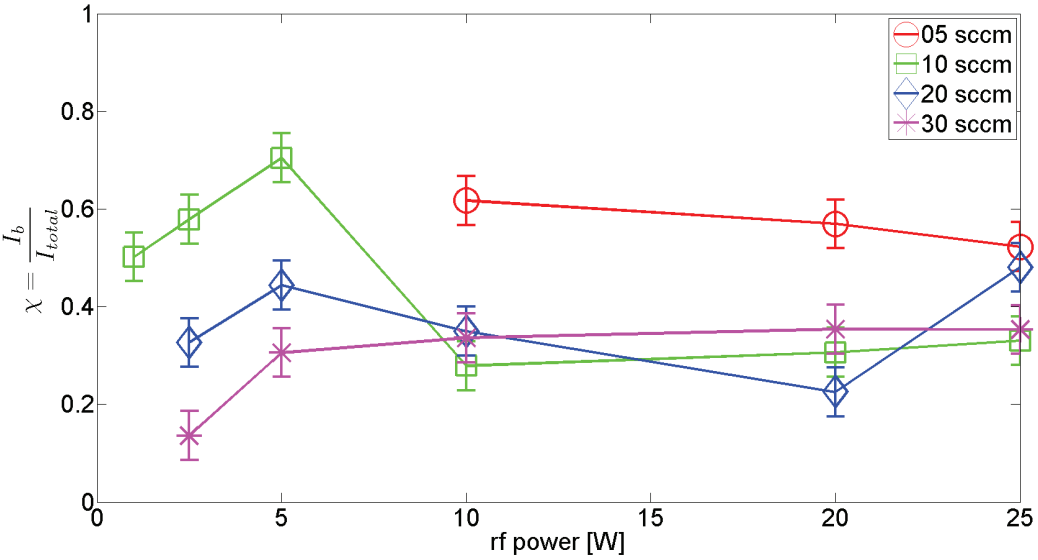

(b)

Figure 5.9: (a) Ideal thrust was calculated for various propellant mass flow rates and rf power levels from ion beam current with the ICP source operating at 710 MHz and an electrostatic grid separation of $d = 2.02$ mm. (b) A figure of merit was calculated for various propellant mass flow rates and rf power levels from the measured ion beam current and grid currents with the ICP source operating at 710 MHz and an electrostatic grid separation of $d = 2.02$ mm.

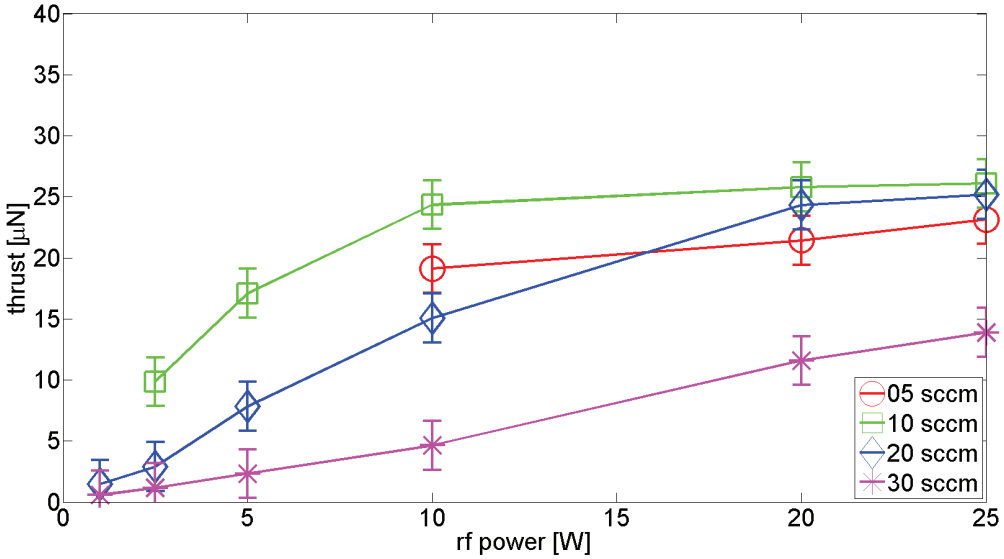

(a)

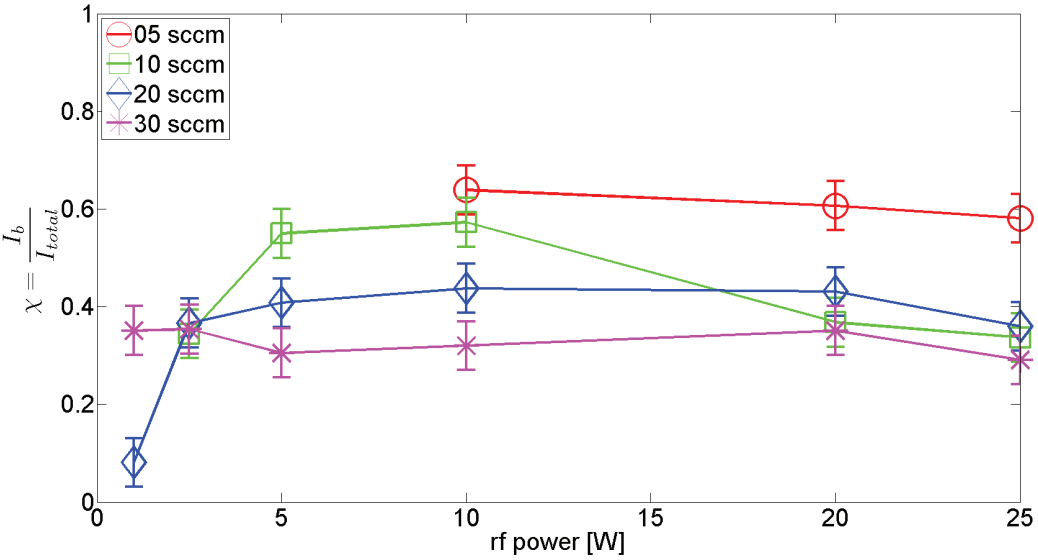

(b)

Figure 5.10: (a) Ideal thrust was calculated for various propellant mass flow rates and rf power levels from ion beam current with the ICP source operating at 730 MHz and an electrostatic grid separation of $d = 2.02$ mm. (b) A figure of merit was calculated for various propellant mass flow rates and rf power levels from the measured ion beam current and grid currents with the ICP source operating at 730 MHz and an electrostatic grid separation of $d = 2.02$ mm.

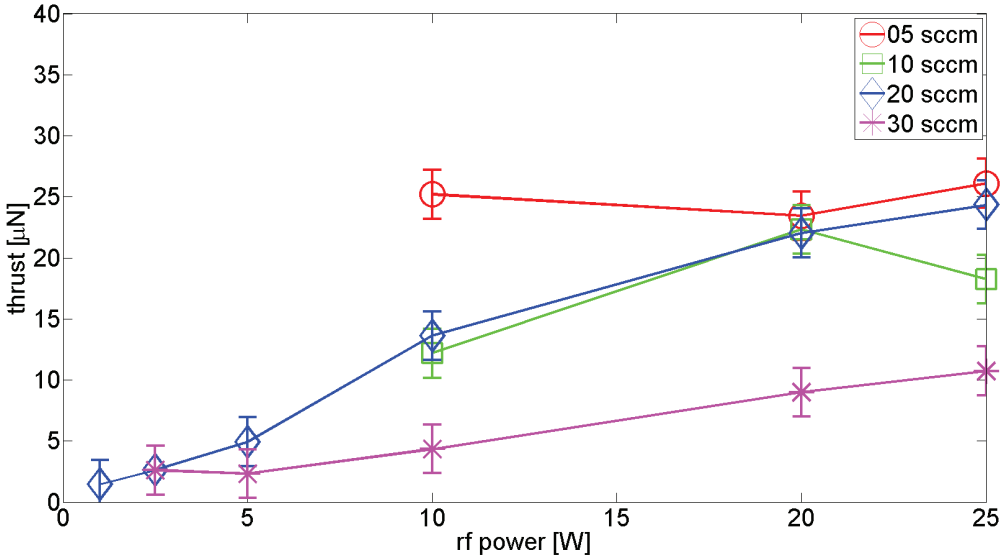

(a)

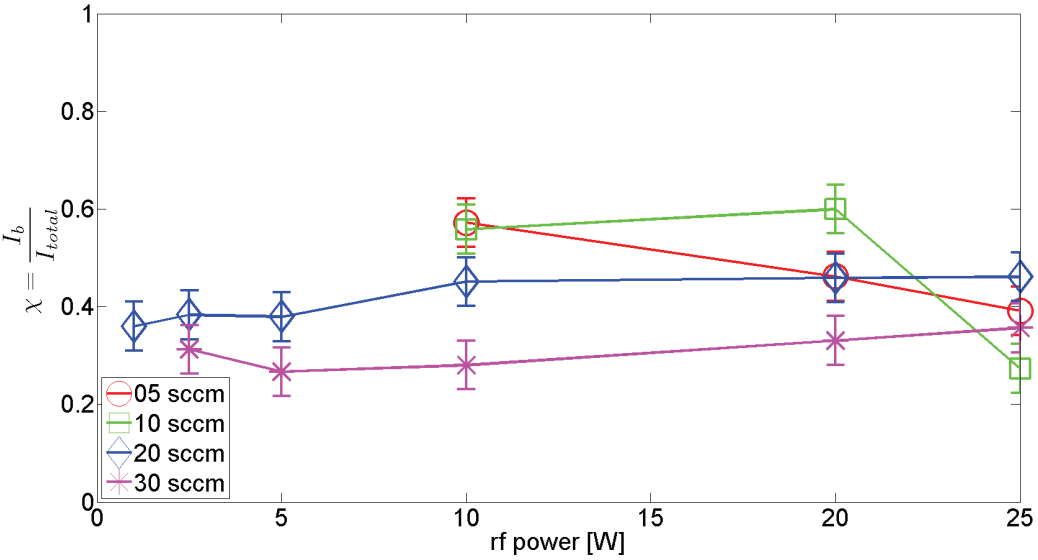

(b)

Figure 5.11: (a) Ideal thrust was calculated for various propellant mass flow rates and rf power levels from ion beam current with the ICP source operating at 750 MHz and an electrostatic grid separation of $d = 2.02$ mm. (b) A figure of merit was calculated for various propellant mass flow rates and rf power levels from the measured ion beam current and grid currents with the ICP source operating at 750 MHz and an electrostatic grid separation of $d = 2.02$ mm.

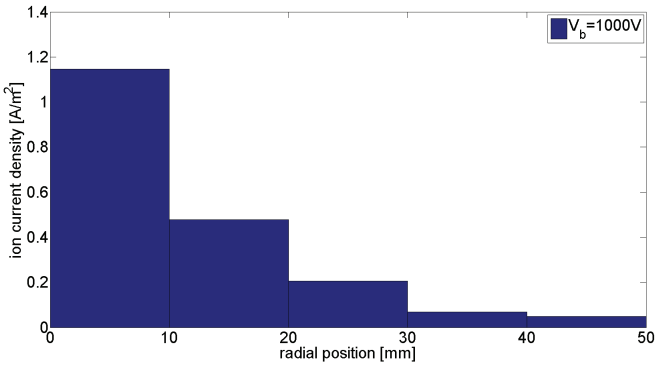

(a)

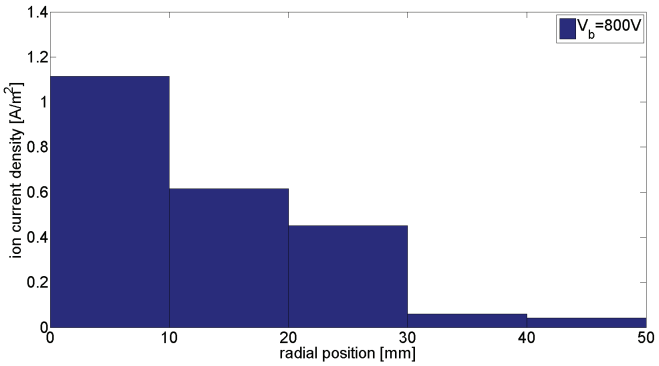

(b)

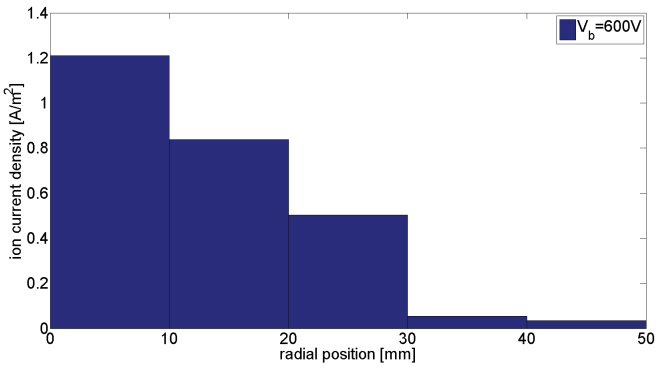

(c)

Figure 5.12: Ion beam current density versus radial position for various beam voltages: (a) 1000 V, (b) 800 V, and (c) 600 V. Each bar represents a pad on the segmented collector.

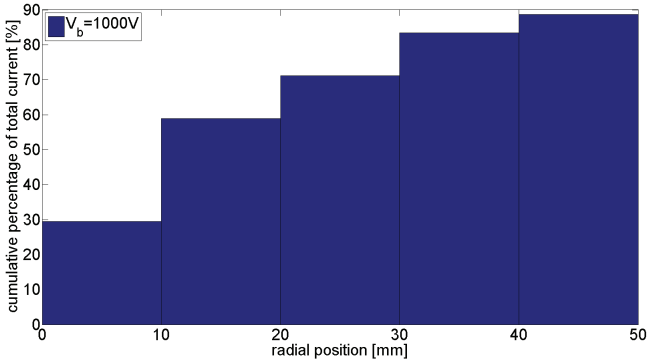

(a)

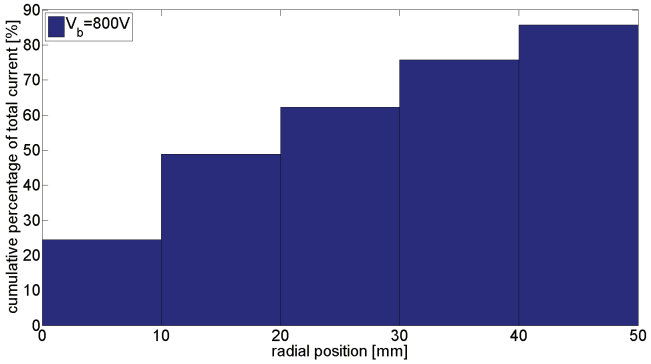

(b)

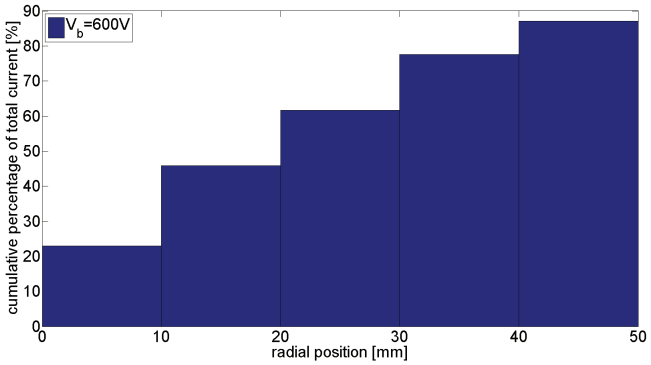

(c)

Figure 5.13: Cumulative percentage of total ion current density versus radial position for (a) $V_b = 1000\,\mathrm{V}$, (b) $V_b = 800\,\mathrm{V}$, and (c) $V_b = 600\,\mathrm{V}$.

CHAPTER 6

CONCLUSION

A summary of results, discussion, and recommendations for future work are presented in this final chapter.

6.1 Summary of Results

A miniature rf ion thruster with an inductively coupled plasma source was analyzed. The thruster has a diameter of 2 cm and a length of 4.5 cm. The thruster was tested at various propellant flow rates (0.1, 1, 2.5, 5, and 10 sccm) and rf powers (1, 2.5, 5, 10, 20, and 25 W) at three different frequencies (710, 730, and 750 MHz). After determining the optimum operating conditions of the thruster, a thrust of 22.35 μN and a specific impulse of 15.31 s were obtained 5 W of rf power at 730 MHz, propellant flow rate of 5 sccm, and an ion net acceleration voltage of 1000 V. With a beam divergence angle of 26.25° and the assumption of a single charged ion species, the total thrust correction factor was 0.90. At these conditions, the mass utilization efficiency of the thruster was calculated to be 0.24 %. The electrical efficiency of thruster was calculated to be 16.94 % with an electron-ion energy pair cost of 5.9 keV/ion. The over all efficiency of the thruster was calculated to be 0.033 %.

6.2 Discussion

Because of the high propellant mass flow rates needed to sustain the plasma at low background pressures of 1×10^{-5} Torr, the mass utilization efficiency and specific impulse were extremely low. In order to become a more efficient thruster, the propellant flow rate must be lowered dramatically ($\approx$ 0.1 sccm). It is important to note that the performance of the ICP source degraded significantly between the time Experiment 1 and Experiment 2 were performed. Running the thruster in the Experiment 2 setup caused the electrostatic grids and ion collector plate to sputter, and the material was deposited inside the discharge chamber and on the ICP source. If the propellant mass flow rate can be lowered to 0.1 sccm, η_m should increase by a factor of 50 if 0.86 mA of ion beam current from the optimum operating condition from Experiment 2 is maintained. It is also noteworthy that an increase in ion beam will also increase η_m.

The electrical efficiency was higher than the mass utilization efficiency, but still less than desired. In order to increase η_e, the ion beam power needs to be maximized while the rf input power and power supplies (ion optics, neutralizer, etc.) are minimized. The ion beam current can be increased by increasing the electrical transparency of the electrostatic grids. This increase in transparency will most likely call for more holes in the grids and possibly an increase in thruster diameter.

With low mass utilization and electrical efficiencies, the overall total efficiency of the thruster was extremely low (0.033 %). Other than increasing the mass utilization and electrical efficiencies, the thrust correction factors can be increased. The ion beam divergence angle for the thruster at the optimum operating condition was 26.25°, which translates to a 10.31 % loss of thrust. A beam divergence angle of $< 10°$

is desirable (less than a 2 % loss of thrust). The ion beam divergence angle can be minimized by optimizing the design of the electrostatic grids through the use of computer simulation.

The original thrust goal of the thruster was 200 μN. Using Equation 2.8, the minimum ion beam current need for a thrust of 200 μN with a net ion acceleration voltage of 1000 V is 6.9 mA. It is suspected that the sputtering of the grids and collector plate during Experiment 2 degraded the performance of the ICP source to the point where an ion beam greater than 0.86 mA could not be produced without extinguishing the plasma.

6.3 Recommendations for Future Work

Recommendations for future work are enumerated below.

1. Optimization of the ion optics would yield greater electrical efficiency, minimal ion beam divergence, and greater total efficiency.

2. Propellant delivery needs to be investigated further. Lower flow rates, while maintaining current local gas pressures, are needed in order increase the mass utilization efficiency of the thruster. Injecting propellant axially may be causing low ionization efficiency. Lateral gas injection with multiple gas inlets may be a solution.

3. The electrostatic grids should be constructed of, or coated with, a material with a low secondary electron yield and more resistant to sputtering than stainless steel. Molybdenum, titanium, and tantalum would be candidates for this material.

4. Just as with the electrostatic grids, the segmented collectors should be constructed with a material that resists sputtering better than silver.

5. Single device integration needs to be done when the optimum design is reached. This involves moving from modular LTCC pieces (ICP source, discharge chamber, and electrostatic grids) to permanently attached LTCC pieces. Electrical wiring for the grids will also be embedded in the ceramic of the discharge chamber. The thruster also needs a grounded electrostatic shield around it.

6. Electronics for the rf system, grid power supplies, and propellant delivery need to be developed and scaled down from their laboratory counterparts for use on a small satellite. The rf supply will also float slightly more positive than the screen grid and the grids will be biased at the appropriate potentials for in-space operation.

7. A neutralizer needs to be included for use in space. The neutralizer will most likely require another power supply and needs to be calibrated to emit the correct amount of electron current in order to completely neutralize the ion beam.

8. Thrust should also be measured mechanically using the micronewton thrust measurement stand Woldvedt [49]. These results can then be compared to the electrical thrust measurements.

9. The ICP source can be integrated into other types of thrusters such as pulsed inductive thruster (PIT) [50] as a pre-ionizer.

REFERENCES

[1] Futron Corporation, "Space transportation costs: trends in price per pound to orbit 1990-200," Tech. Rep., 2002.

[2] United States Department of Labor Bureau of Labor Statistics, *CPI Inflation Calculator*. [Online]. Available: `http://www.bls.gov/data/inflation_calculator.htm`.

[3] M. Rycroft and N. Crosby, Eds., *Smaller Satellites: Bigger Business?* Kluwer Academic Publishers, 2002, pp. 1–19.

[4] R. J. Cybulski, D. M. Shellhammer, R. R. Lovell, E. Domino, and J. T. Kotnik, "Results from SERT I ion rocket flight test," National Aeronautics and Space Administration Glenn Research Center (formerly Lewis Research Center), Tech. Rep., 1965.

[5] R. Killinger, H. Bassner, G. Kienlein, and J. Müller, "Electric propulsion system for ARTEMIS," in *The 26th International Electric Propulsion Conference*, Kitakyushu, Japan, 1999.

[6] J. R. Brophy, M. A. Etters, J. Gates, C. E. Garner, M. Klatte, C. J. Lo, M. G. Marcucci, S. Mikes, M. Mizukami, B. Nakazono, and G. Pixler, "The Dawn ion propulsion system- getting to launch," in *The 30th International Electric Propulsion Conference*, Florence, Italy, 2007.

[7] R. H. Goddard, *The Green Notebooks*, Vol. 1. The Dr. Robert H. Goddard Collection at Clark University Archives, Clark University, Worcester, MA, 1906, p. 84.

[8] R. H. Goddard, "Method of and means for producing electrified jets of gas," Patent 1 363 037, Dec. 1920.

[9] K. E. Tsiolkovsky, *Works on Rocket Technology*. Publishing House of the Defense Industry, 1947.

[10] E. Y. Choueiri, "A critical history of electric propulsion: the first 50 years (1906-1956)," *Propulsion and Power*, vol. 20, no. 2, pp. 193–203, 2004.

[11] H. J. Oberth, *Wege zur Raumschiffahrt*. Druck und Verlag von R. Olden-bourg, 1929, (in German).

[12] E. Stuhlinger, *Electric Propulsion for Space Flight*. McGraw-Hill, 1964.

[13] H. R. Kaufman, "Ion-thruster propellant utilization," National Aeronautics and Space Administration Glenn Research Center (formerly Lewis Research Center), Tech. Rep., 1971.

[14] Radio Corporation of America Astro-Electronics Division, "Summary report on the development of the SERT I spacecraft," National Aeronautics and Space Administration Glenn Research Center (formerly Lewis Research Center), Tech. Rep., 1966.

[15] J. Polk, D. Brinza, R. Kakuda, J. Brophy, I. Katz, J. Anderson, V. Rawlin, M. Patterson, J. Sovey, and J. Hamley, "Demonstation of the NSTAR ion propulsion system on the deep space one mission," in *The 27th International Electric Propulsion Conference*, Pasadena, CA, 2001.

[16] C. Edwards, N. Wallace, C. Tato, and P. van Put, "The T5 ion propulsion assembly for drag compensation on goce," in *Second International GOCE User Workshop "The Geoid and Oceanography"*, Frascatti, Italy, 2004.

[17] H. Kuninaka, K. Nishiyama, I. Funakai, Tetsuya, Y. Shimizu, and J. Kawaguchi, "Asteroid rendezvous of HAYABUSA explorer using microwave discharge ion engines," in *The 29th International Electric Propulsion Conference*, Princeton University, 2005.

[18] R. Killinger, R. Kukies, M. Surauer, A. Tomasetto, and L. van Holtz, "ARTEMIS orbit raising inflight experience with ion propulsion," *Acta Astronautica*, vol. 53, no. 4-10, pp. 607–621, 2003.

[19] NASA/JPL-Caltech. [Online]. Available: `http://nmp.jpl.nasa.gov/ds1/images.html`.

[20] [Online]. Available: `http://dawn.jpl.nasa.gov/mission/timeline.asp`.

[21] ——, [Online]. Available: `http://dawn.jpl.nasa.gov/multimedia/images/Dawn_FarewellPortrait_lg.jpg`.

[22] R. Wirz, J. Polk, Collen, Marrese, J. Mueller, J. Escobedo, and P. Sheehan, "Development and testing of a 3cm electron bombardment micro-ion thruster," in *The 27th International Electric Propulsion Conference*, Pasadena, CA, 2001.

[23] V. F. Mistoco, T. A. Trudel, S. Bilén, and M. M. Micci, "Vacuum testing of the miniature radio-frequency ion thruster," in *The 29th International Electric Propulsion Conference*, Princeton University, 2005.

[24] T. A. Trudel, S. G. Bilén, and M. M. Micci, "Design and performance testing of a 1-cm miniature radio-frequency ion thruster," *Journal of Propulsion and Power*, vol. 39, no. 11, pp. 1–2, 2012.

[25] D. Feili, D. M. Di Cara, H. J. Leiter, J. G. Del Amo, H. W. Loeb, S. Weis, D. Kirmse, P. E. Frigot, M. Orlandi, H. Mü, and B. K. Meyer, "The μNRIT-4 ion engine: a first step towards a european mini-ion engine system development," in *The 30th International Electric Propulsion Conference*, Florence, Italy, 2007.

[26] D. Feili, B. Lotz, S. Bonnet, B. K. Meyer, H. W. Loeb, and N. Puetmann, "The μNRIT-2.5- a new optimized microthruster of giessen university," in *The 31st International Electric Propulsion Conference*, Ann Arbor, Michigan, United States, 2009.

[27] C. M. Collingwood, S. B. Gabriel, M. H. Corbett, N. C. Wallace, and P. Jameson, "Development of a differential radio frequency ion thruster for precision spacecraft contro,l," *Journal of Plasma and Fusion Research*, vol. 8, pp. 1564–1568, 2009.

[28] S. Christensen, "Modeling and measuring the characteristics of an inductively coupled plasma antenna for a micro-propulsion system," MS, Boise State University, Boise, ID, USA, 2012.

[29] S. Christensen and J. Browning, "Modeling the characteristics of an inductively coupled plasma antenna for use in a micro-propulsion system," in *The 55th International Midwest Symposium on Circuits and Systems*, Boise, ID, 2012.

[30] K. Nishikawa and M. Wakatani, *Plasma Physics*, 3rd ed. Springer, 2000, p. 11.

[31] M. A. Lieberman and A. J. Lichtenberg, *Principles of Plasma Discharges and Materials Processing*, 2nd ed. Wiley, 2005, pp. 535–536.

[32] ——, *Principles of Plasma Discharges and Materials Processing*, 2nd ed. Wiley, 2005, pp. 387–390.

[33] ——, *Principles of Plasma Discharges and Materials Processing*, 2nd ed. Wiley, 2005, pp. 461–469.

[34] J. Browning, C. Lee, D. Plumlee, S. Shawver, S. M. Loo, M. Yates, M. McCrink, and J. Taff, "A miniature inductively coupled plasma source for ion thrusters," *Plasma Science, IEEE Transactions on*, vol. 39, no. 11, pp. 3187 –3195, 2011.

[35] G. P. Sutton and O. Biblarz, *Rocket Propulsion Elements*, 8th ed. John Wiley & Sons, 2010, p. 7.

[36] D. M. Goebel and I. Katz, *Fundamentals of Electric Propulsion: Ion and Hall Thrusters*. Wiley, 2008.

[37] M. A. Lieberman and A. J. Lichtenberg, *Principles of Plasma Discharges and Materials Processing*, 2nd ed. Wiley, 2005, pp. 176–177.

[38] D. H. Mundy, "Factors affecting the beam divergence of a T5 ion engine," in *The 25th International Electric Propulsion Conference*, Cleveland, Ohio, 1997.

[39] DuPont, *951 Green Tape*. [Online]. Available: `http://www2.dupont.com/MCM/en_US/assets/downloads/prodinfo/951LTCCGreenTape.pdf`.

[40] [Online]. Available: `http://www.comsol.com/`.

[41] P. P. Bumbarger, J. Browning, and D. Plumlee, "Simulation and experimental analysis of a miniature ion thruster fabricated in low temperature co-fired ceramic," in *The 39th IEEE International Conference on Plasma Science*, Edinburgh, Scotland, 2012.

[42] J. Taff, M. Yates, C. Lee, S. Shawver, J. Browning, and D. Plumlee, "Fabrication of an inductively coupled plasma antenna in low temperature co-fired ceramic," *International Journal of Applied Ceramic Technology*, vol. 10, no. 2, pp. 321–329, 2012.

[43] K. Parish, M. Yates, D. Reis, D. Plumlee, and J. Taff, "Characterization of the fabrication process of rolled LTTC structures," *International Journal of Applied Ceramic Technology*, vol. 10, no. 3, pp. 458–467, 2013.

[44] USGS, *Boise south topographical map*, www.usgs.gov, 2010.

[45] *Ionization gauge/ dual convection with inegrated controller and display 392 series ionization vacuum gauge*, Rev. 1.09, Kurt J. Lesker Company, 2009.

[46] M. A. Lieberman and A. J. Lichtenberg, *Principles of Plasma Discharges and Materials Processing*, 2nd ed. Wiley, 2005, pp. 185–195.

[47] P. P. Bumbarger, J. Browning, and D. Plumlee, "Langmuir probe characterization of a miniature inductively coupled plasma source for ion thrusters," in *The 40th IEEE International Conference on Plasma Science*, San Francisco, California, 2013.

[48] [Online]. Available: `http://www.fluidat.com/`.

[49] J. T. Woldvedt, "The design, fabrication, and calibration of a micro-newton thrust measurement stand," MS, Boise State University, Boise, ID, USA, 2011.

[50] A. K. Hallock, "Effect of inductive coil geometry on the operating characteristics of a pulsed inductive plasma accelerator," PhD thesis, Princeton University, Princeton, NJ, USA, 2012.